Crosstalk suppression of parallel gates for fault-tolerant quantum computation with trapped ions via optical tweezers

Lin Cheng,[1,2] Sheng-Chen Liu,[1] Liang-You Peng,[1,2,3,*] and Qihuang Gong[1,2,3]

[1] *State Key Laboratory for Mesoscopic Physics and Frontiers Science Center for Nano-optoelectronics, School of Physics, Peking University, Beijing 100871, China*

[2] *Beijing Academy of Quantum Information Sciences, Beijing 100193, China*

[3] *Collaborative Innovation Center of Extreme Optics, Shanxi University, Taiyuan 030006, China*

(Received 2 April 2024; revised 26 July 2024; accepted 16 August 2024; published 10 September 2024)

The ability to perform entangling operations in parallel with a low error is essential for a large-scale fault-tolerant quantum computer. However, for trapped-ion systems, it is a challenging task due to the crosstalk resulting from the collective motional modes. Here, we develop a highly paralleled quantum circuit demonstrating a logical qubit based on the Steane code and study the impact of the crosstalk error on the performance of the fault-tolerant protocol. We show that the crosstalk indeed greatly destroys the fault-tolerant property of the quantum error correction. To achieve the break-even point with encoded qubits, we identify the suppression requirement of the crosstalk error to be less than 10^{-6} for the Steane code. Furthermore, to mitigate the crosstalk below the fault-tolerant threshold, we propose a highly efficient optimization scheme by utilizing the programmable optical tweezer array. Overall, we make an elegant combination of the pulse-control optimization of parallel gate operations with the fault-tolerant protocol on the error-protected universal quantum computer.

DOI: 10.1103/PhysRevApplied.22.034021

I. INTRODUCTION

Large-scale quantum computers have the potential to solve some key computational problems that are beyond the capabilities of classical computers, such as quantum simulation of complex quantum systems, prime factorization, and others [1,2]. However, the execution of large-scale, useful algorithms on quantum processors requires very low gate-error rates that are currently unachievable due to imperfect control and noise in gate operations. To address this challenge, quantum error correction (QEC) [3–6] has been proposed to protect quantum information against noise with the circuit design principle of quantum fault tolerance. The key ingredient is QEC codes that redundantly encode quantum information into a protected subspace within a larger Hilbert space of many physical qubits, such that if any given physical qubit fails, it does not corrupt the underlying logical information. In principle, with sufficiently low physical error rates, which lie below the critical threshold of the corresponding QEC code, i.e., the break-even point, arbitrary levels of protection can be achieved while employing active detection and correction of errors and using a polynomially scaling number of physical qubits.

The trapped-ion system [7–9] is one of the leading technology platforms for achieving a universal large-scale, fault-tolerant (FT) quantum information processor due to many beneficial and unique characteristics, such as the longest coherence time [10], and the high-fidelity single-qubit [11], two-qubit [12–14], or multiqubit entangling gates [15–19]. With these superior features, some central elements of QEC have been demonstrated, such as logical state preparation [20], FT stabilizer measurement [21], FT operation of one logical qubit [22], universal gate sets [23,24], as well as repetitive QEC cycles [25–27]. However, the parallel implementation of two-qubit quantum gates in a linear ion chain has not been studied in general with the full consideration of these necessary aspects.

To achieve an efficient error correction, the quantum circuit of a complete QEC cycle requires numerous physical qubits and entangling gates, which typically implies a substantial resource overhead. A major concern is the proliferation of errors for qubits that suffer from high idle errors [28,29]. Therefore, quantum gate parallelism can significantly reduce the depth of quantum circuits and then substantially decrease the resource requirements for fault tolerance [15–19]. However, simultaneously implementing multiple gates commonly shows worse performance for trapped-ion systems [15]. Generally, this degradation is attributed to the unwanted interactions among qubits

*Contact author: liangyou.peng@pku.edu.cn

of different gates, i.e., the crosstalk, which results from all-to-all interactions of the ion chain and the corresponding collective motional modes [8,19].

Note that the crosstalk of parallel gates in this work is different from another noisy process, which is also called "crosstalk," caused by the leakage light from the tightly focused laser beam to the neighboring ions [29–31]. Previous studies show that the crosstalk stems from imperfect addressing has a harmful effect on the performance of the QEC protocol and break the fault tolerance [29,30]. Recently, some experimental groups [32–34] have demonstrated that the optical addressing crosstalk can be effectively mitigated below the FT threshold, which was derived in Ref. [30]. In this case, the crosstalk of parallel gates is one of the major error sources in parallel FT quantum circuit which can cause not just increased gate errors but even a variety of correlated errors. Furthermore, it will significantly impair the reliability of the whole algorithm and the realization of FT quantum computing. Additionally, the error probability of crosstalk of parallel gates is larger in a parallelized quantum circuit.

In this work, we develop a trapped-ion QEC protocol of a logical qubit protected by the Steane code and present a comprehensive study of the crosstalk errors. In particular, the quantum gate operations in FT quantum circuit construction are highly parallelized. As depicted in Fig. 1(a), the QEC protocol consists of several central FT blocks, which correspond to initialize logical states, make the syndrome extraction, detect and correct errors, and determine logical measurement outcomes. Taking the essential ingredient—the syndrome extraction [35–37]—as an example, our scheme allows the simultaneous measurement of three stabilizers in Fig. 1(b) and then all six stabilizers can be measured in two rounds, especially for the unflagged stabilizer syndrome. Rather than measuring only one stabilizer at a time sequentially [38], extracting multiple syndromes in parallel can drastically decrease the number of quantum gates and measurement rounds, and in turn lower the error probability of idle qubits [39].

To figure out the crosstalk impact on QEC, we introduce theoretical models describing these noises and then assess the performance of FT protocols of encoded qubits with respect to bare physical qubits. Our detailed study shows the destructive effect of crosstalk on the QEC protocol as it can induce error processes affecting groups of physical data qubits. Moreover, we estimate the accuracy requirements of the crosstalk suppression for parallel gates to reach the break-even point of FT advantage, i.e., identify for which physical error parameters, the infidelity of logical state is lower than their respective physical qubit counterparts. Therefore, for QEC to be helpful in computation and demonstrating the advantage of parallel execution, the crosstalk error should be adequately accounted for in parallel FT quantum circuit and suppressed to below the FT threshold.

For superconducting qubits, there are a lot of analyses to characterize the quantum crosstalk of the simultaneous gate operations [40–42]. Here, we focus on the trapped-ion systems. For this platform, several schemes of low-crosstalk parallel quantum gates with a few qubits have been demonstrated [15,18] and some preliminary theoretical attempts have been made for long ion chains [17,19,43,44]. In Ref. [18], an exact protocol for parallel gates has been devised, which demands enough pulse segments of the equally segmented method. In Ref. [43], the authors have made use of optical tweezers with the same intensity for parallel two-qubit entangling gates. However, the mitigation of crosstalk in these schemes commonly require complex pulse shape, thus placing heavy resource burdens on the control system and limiting their feasibility for large-scale FT quantum computing. Additionally, to find a high-quality solution is extremely difficult by either the analytic methods or the numerical optimization techniques because of the nonlinear constraints for crosstalk terms.

In our work, we provide an efficient optimization method to design high-fidelity and low-crosstalk parallel gates based on the optical tweezer array that can suppresses the crosstalk directly below the FT threshold at the gate level in Figs. 1(c) and 1(d). The optical tweezer [43–46] is commonly utilized as a powerful tool in quantum simulation [47] and scalable quantum computation [43,44]. Here, we adopt the programmable tweezer array with different intensities to decrease the constraints of crosstalk. As shown in Fig. 1(c), the motional modes of the ion chain in the presence of optical tweezer are localized instead of collective and the corresponding mode frequencies are split into several subsets. On the basis of the localized modes and gapped mode frequencies, we just need extremely simple pulse shape, and then can effectively suppress the crosstalk terms of parallel gate group below the FT threshold as depicted in Fig. 1(d). Of note, the parallel gates based on tweezer arrays are quite flexible due to the features of controllable optical intensity, dynamically reconfiguring the tweezer array and fast optical switching. And then we can achieve different parallel entangling gate groups in a QEC cycle in Fig. 1(a). In terms of the numerical optimization method, our optimization scheme can quickly find a satisfied confinement of the tweezer array based on a presearch technique compared with the traditional numerical optimization techniques.

The rest of this paper is organized as follows: In Sec. II, we give a brief introduction of the set of gates and the noise model in a trapped-ion toolbox. In Sec. III, we present in detail the QEC protocol with a highly parallelized FT quantum circuit. In Sec. IV, we assess the

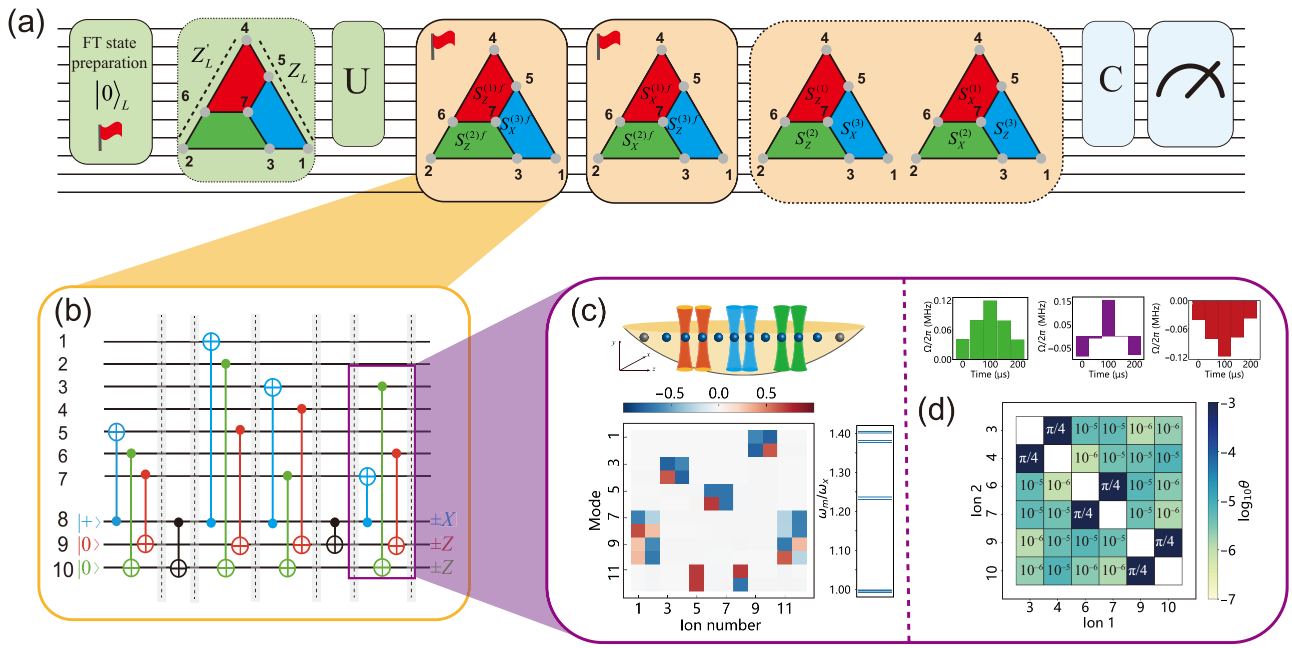

FIG. 1. Schematic diagram of the QEC protocol based on high-quality parallel two-qubit gates with programmable optical tweezer array. (a) The QEC cycle, which includes the FT logical state preparation with parallel gates (green blocks), the parallel syndrome extraction protocol (orange blocks), and the decoder and measurement (blue blocks). (b) The quantum circuit of the first parallel flagged syndrome extraction of the stabilizers $\{S_X^{(3)f}, S_Z^{(1)f}, S_Z^{(2)f}\}$ in (a). (c) The design of parallel two-qubit quantum gate group (purple dashed box) shown in (b) based on optimized optical tweezer array. The $^{171}Yb^{+}$ ion chain with pinned ion pairs of different tweezer intensities (top) and the localized transverse motional modes and the gapped mode frequencies (bottom) are shown. The oscillation amplitude and direction of ions are represented by the color of the squares. (d) The simple pulse shape of the three ion pairs are plotted in the top. The crosstalk values for each ion pair are shown at the bottom. Both axes represent the numbering of the pinned ions.

performance of the FT protocol under the noises considered and identify the FT threshold of crosstalk suppression for parallel gates. Then, we propose an efficient optimization scheme to achieve the parallel two-qubit gates with infidelity and crosstalk below the FT threshold based on an optical tweezer array in Sec. V. And in Sec. VI, we discuss the optimized results of the high-quality parallel tweezer gates in a chain of 12 $^{171}Yb^{+}$ ions. Finally, we summarize our main results and give an outlook in Sec. VII.

II. TRAPPED-ION TOOLBOX FOR QEC

In this scheme, we focus on a same-species linear ion chain of 12 ions for $^{171}Yb^{+}$ in which physical qubits are encoded into hyperfine "clock" states of ions [8]. In the following, we will discuss the set of physical gates for data qubits and the noise processes of the device.

A. The set of quantum gates

1. Theoretical model of single-qubit quantum gates

The single-qubit rotations in trapped-ion systems can be realized by a laser pulse resonant to the qubit transition with variable phase and pulse area [48]. The unitary evolution operator can be expressed as $R_\phi^i(\theta) = \exp[-i\frac{\theta}{2}(\hat{\sigma}_x^i\cos\phi + \hat{\sigma}_y^i\sin\phi)]$, where $\hat{\sigma}_x^i = X_i$ and $\hat{\sigma}_y^i = Y_i$ are single-qubit Pauli operators acting on ith ion. The rotation angle θ is controlled via the duration and intensity of the laser pulse, and the angle of the rotation axis with respect to the X axis ϕ is controlled via the pulse phase. In this work, single-qubit gates also operate in parallel in the quantum circuit of the QEC protocol and it is easy to prevent the crosstalk of parallel single-qubit gates. Therefore, in the following, we will ignore the crosstalk effect of parallel single-qubit gates.

2. Theoretical model of parallel two-qubit quantum gates

For entangling operations, a popular and widely used two-qubit entangling gate is known as the Mølmer-Sørensen (MS) gate [49–51], which are mediated by the collective motional modes through spin-dependent optical forces. Here, we focus on an efficient approach in which the optical forces simultaneously couple to all modes [50–52] instead of a single mode [49]. The optical forces are realized by shining two counterpropagating beams on the ions, with an equal but opposite detuning μ in the neighborhood of the motional mode frequencies.

The time evolution operator of a single MS gate on ion pair $[j, j']$ at gate duration τ is given by [50,52]

$$\hat{U}_{j,j'}(\tau) = \exp\left\{\sum_{j,m}(\alpha_j^m(\tau)\hat{a}_m^\dagger - \alpha_j^{m*}(\tau)\hat{a}_m)\hat{\sigma}_x^j + i\sum_{j<j'}\theta_{j,j'}(\tau)\hat{\sigma}_x^j\hat{\sigma}_x^{j'}\right\}, \tag{1}$$

where $\hat{a}_m^\dagger$ and $\hat{a}_m$ are, respectively, the creation and the annihilation operators acting on the mth mode. And the residual spin-motion coupling $\alpha_j^m(\tau)$ is given by

$$\alpha_j^m(\tau) = -i\eta_j^m\int_0^\tau \Omega_j(t)\sin(\mu_j t)e^{i\omega_m t}\,dt, \tag{2}$$

where μ_j is the laser detuning and $\Omega_j(t)$ is the Rabi frequency of the jth ion. The coupling strength $\theta_{j,j'}(\tau)$ between the jth and j'th ion for pair $[j, j']$ is given by

$$\theta_{j,j'}(\tau) = 2\sum_m \eta_j^m\eta_{j'}^m\int_0^\tau dt_2\int_0^{t_2} dt_1\Omega_j(t_2)\Omega_{j'}(t_1) \times \sin(\mu_j t_1)\sin(\mu_{j'} t_2)\sin[\omega_m(t_1 - t_2)], \tag{3}$$

where the Lamb-Dicke (LD) parameter $\eta_j^m = b_j^m\Delta k_j\sqrt{\frac{\hbar}{2m_{\text{ion}}^j\omega_m}}$ couples the jth ion with the mth mode, where b_j^m is the mode eigenvector for mode frequency ω_m, Δk_j is the difference of two wave vectors, and m_{ion}^j is the mass of the jth ion. The lasers have a wavelength around $\lambda = 355$ nm for the qubit transitions of $^{171}\text{Yb}^+$. In Eq. (3), the summation over m is limited to the transverse x modes, which is preferable for entangling operations due to less susceptibility to the heating [51].

For a successful completion of an entangling operation $U_{j,j'} = \text{MS}(-\frac{\pi}{2}) = \exp(i\frac{\pi}{4}\hat{\sigma}_x^j\hat{\sigma}_x^{j'})$, the following constraints should be satisfied:

$$\alpha_j^m(\tau) = 0, \quad \forall j, m, \tag{4}$$

$$\theta_{j,j'}(\tau) = \pi/4. \tag{5}$$

In previous studies, amplitude-modulated (AM) gates [49–51], phase-modulated (PM) gates [53–55], frequency-modulated (FM) gates [56–58], and their combinations [59,60] have been developed and demonstrated in a discrete or continuous way to fulfill the above-mentioned constraints.

In the present work, we adopt the discrete AM method [50–52], where τ is equally divided into N_{seg} segments. We define a real column vector $\mathbf{\Omega} = (\Omega_1, \Omega_2, \ldots, \Omega_{N_{\text{seg}}})^T$ and the amplitude in each segment is independently modulated. The matrix form of the constraints in Eqs. (4) and (5) can be given as follows:

$$\mathbf{M}^j\mathbf{\Omega}^j = \mathbf{0}, \tag{6}$$

$$\theta_{j,j'}(\tau) = (\mathbf{\Omega}^j)^T\mathbf{D}^{[j,j']}\mathbf{\Omega}^{j'}, \tag{7}$$

where $\mathbf{M}^j$ is the $2N \times N_{\text{seg}}$ real coefficient matrix, $\mathbf{D}^{[j,j']}$ is the $N_{\text{seg}} \times N_{\text{seg}}$ matrix, and $\mathbf{\Omega}^j$ is the amplitude vector of length N_{seg} of the jth qubit. The explicit expressions of $\mathbf{M}^j$ and $\mathbf{D}^{[j,j']}$ are given in Refs. [19,61]. As can be seen, the spin-motion decoupling constraints are linear with respect to the laser amplitude, while the coupling strength constraint is quadratic. The pulse shapes are determined by minimizing the spin-motion decoupling under the quadratic constraint, Eq. (7). For this purpose, we use the method of Lagrange multiplier to solve this generalized eigenvalue problem (see Appendix A for details).

In our scheme, the circuit design of QEC protocol allows for parallel execution of gate operations, as a simultaneous illumination of up to many ion pairs is possible. The evolution operator of the system involving N_1 independent pairs of qubits in a chain of N ions ($N \geq 2N_1$) at τ is given by [15,18]

$$\hat{U}(\tau) = \prod_{[j,j']} U_{j,j'} = \exp\left\{\sum_{j=0}^{2N_1}\sum_{m=0}^{N}(\alpha_j^m(\tau)\hat{a}_m^\dagger - \alpha_j^{m*}(\tau)\hat{a}_m)\hat{\sigma}_x^j + i\sum_{j<j'}^{2N_1}\theta_{j,j'}(\tau)\hat{\sigma}_x^j\hat{\sigma}_x^{j'}\right\}. \tag{8}$$

To perform ideal-fidelity and no-crosstalk N_1 parallel entangling operations in a chain of N ions, we require

$$\alpha_j^m(\tau) = 0, \quad \forall j, m, \tag{9}$$

$$\theta_{j,j'}(\tau) = \begin{cases}\pi/4, & [j,j'] \in J; \\ 0, & [j,j'] \in J',\end{cases} \tag{10}$$

where J is the group of N_1 pairs of ions on which parallel gates are to be performed and the group J' contains all ordered pairs that are not included in J, whose interactions represent crosstalk. Hence, there are a total number of $4N_1 \times N + 2N_1(2N_1 - 1)/2$ constraints to be satisfied [15,16]. Moreover, entangling more pairs in parallel enlarges the problem size quadratically, which set an upper bound on the scaling. Therefore, it is almost impossible to find analytical solutions to this nonconvex quadratically constrained problem, which is NP hard, in general, and is extremely difficult by the numerical optimization techniques because of the increase of the nonlinear constraints.

To overcome these difficulties, we utilize the flexible optical tweezer array to naturally reduce the number of quadratic constraints for crosstalk terms and propose an efficient optimization method to design high-quality parallel entangling gates as detailed below. In this work, we use two types of gate imperfections to measure the parallel gates' performance, i.e., the infidelity list of parallel gate group $\{\delta F_{[j_i,j_i']}\}$ for $i = 1,2,\ldots,N_1$ and $[j_i,j_i'] \in J$, which is related to the residual spin-motion coupling, and the crosstalk list $\{|C_{[j_i,j_i']}|\}$ with $i = 1,2,\ldots,N_2$ for pairs that contained in J' where $N_2 = 2N_1^2 - 2N_1$ is the number of ion pairs whose interactions represent crosstalk. The infidelity $\delta F_{[j_i,j_i']}$ and crosstalk $C_{[j_i,j_i']}$ can be defined as

$$\delta F_{[j,j']} = \frac{4}{5}\sum_m\left(\left|\alpha_j^m\right|^2 + \left|\alpha_{j'}^m\right|^2\right)(2\bar{n}_m + 1), \tag{11}$$

$$C_{[j,j']} = \theta_{j,j'}, \tag{12}$$

where we take the averaged phonon number of the mth mode $\bar{n}_m \approx 0.5$, which can be easily achieved with the Raman sideband cooling.

These gates allow the implementation of the universal set of unitaries $\{H, S, T, \mathrm{CNOT}\}$ by using the combinations of MS gate and single-qubit rotations [see Fig. 10(d) in Appendix D for more details].

B. Noise model

Depending on the models used to describe the effects of errors and noises, there exist a wide range of FT thresholds. Meanwhile, a lot of works about a microscopic description of the possible technical imperfections and environmental noise sources in trapped-ion systems have been presented [28,29,38]. In our work, we focus on the advantage of the parallel execution of gate operations in QEC circuit design and then we discuss three types of incoherent noises, dephasing errors on idle qubits, crosstalk errors when multiple gates execute in parallel and MS gate errors, which use the Kraus-operator representation to describe the components of the quantum error channel.

1. Dephasing errors for idle qubits

A fundamental noise process affecting all implementations of physical qubits is idling noise [28,29]. During the QEC cycle, there are a subset of the qubits, which are not affected by the operations, i.e., idle qubits. These qubits suffer mainly dephasing due to their coupling to the environment, e.g., fluctuations in the laser frequency or magnetic field.

We model a single-qubit dephasing error on a state ρ for each idle qubit as temporally and spatially uncorrelated

$$\mathcal{E}_{\text{idle,deph}}(\rho) = (1 - p_{\text{idle}})\rho + p_{\text{idle}} Z\rho Z, \tag{13}$$

where p_{idle} is the physical error probability for the dephasing process on idle qubit and $Z = \hat{\sigma}_z$ is the Pauli matrix. For the incoherent dephasing channel, the Kraus operators are

$$\begin{aligned} K_{\text{idle},0} &= \sqrt{1 - p_{\text{idle}}}\, I, \\ K_{\text{idle},1} &= \sqrt{p_{\text{idle}}}\, Z. \end{aligned} \tag{14}$$

The error probability p_{idle} can be expressed as

$$p_{\text{idle}} = \frac{1}{2}\left[1 - \exp\left(-\frac{t}{T_2}\right)\right], \tag{15}$$

where t is the idle duration of idle qubit and T_2 is the standard parameter quantifying the resilience of the qubit's phase coherence, i.e., coherence time. We employ the experimental value of $T_2 = 200\,\text{ms}$ for the trapped-ion hyperfine qubit of $^{171}\text{Yb}^+$ [8].

2. Two-qubit MS gate errors

High-fidelity single- and two-qubit gates are essential building blocks for a FT quantum computer [8]. While there has been much progress in suppressing single-qubit gate errors for trapped-ion systems [11], two-qubit gates still suffer from error rates that are orders of magnitude higher. In addition, the entangling MS gates are most commonly used to describe QEC circuit and especially are crucial ingredient in the FT stabilizer readout. Therefore, in the following, we will focus only on MS gate errors. We adopt the AM gate in which the segmented laser amplitudes are carefully designed to decouple the internal qubit states from all the motional modes and generate a desirable spin-spin entangling phase.

In previous works, microscopic noise models of MS gates have been derived, considering fluctuations of the laser intensity and phase [38], motional heating [62], or incoherent over-rotations [31], etc. However, for simplicity, we apply depolarizing noise for MS gates, which is considered the most general and architecture-agnostic incoherent noise channel because the fault operators of the depolarizing noise channel form a basis in the space of single- and two-qubit unitaries, respectively. And the depolarizing noise does not perform worse at estimating logical failure rates than an incoherent over-rotation noise model, which consists of the stochastic application of Pauli-type errors [38].

The modeled error channel for depolarizing noise on entangling MS gates reads

$$\mathcal{E}_{\mathrm{dpl}}^{(2)}(\rho) = (1 - p_{\mathrm{MS}})\rho + \frac{p_{\mathrm{MS}}}{15}\sum_{i=1}^{15} E_2^{(i)} \rho E_2^{(i)}, \qquad (16)$$

where

$$E_2 = \{E_k \bigotimes E_l, \forall E_{k,l} \in \{I, X, Y, Z\}\} \backslash \{I \bigotimes I\}. \qquad (17)$$

With an error probability p_{MS}, one of 15 nontrivial weight-two Pauli faults is added to the ideal entangling gate. The relationship between the error probability and the infidelity of physical MS gate is $p_{\mathrm{MS}} = \frac{5}{4}\delta F$.

3. Crosstalk errors of parallel MS gates

As stated above, executing parallel quantum gates is especially advantageous to QEC codes in FT quantum computation. However, the crosstalk between qubits of different MS gates resulting from the collective motional modes will greatly degrade the performance of parallel gates.

When executing N_1-independent pairs of qubits in a chain of N ions, there exist N_2 crosstalk terms. The crosstalk for J' can be expressed as the following form:

$$\hat{U}(C) = \prod_{[j,j'] \in J'} \exp\left(-iC_{[j,j']} X_j X_{j'}\right). \qquad (18)$$

The stochastic version of the crosstalk channel can be described as

$$\mathcal{E}_{\mathrm{c}}(\rho) = \mathcal{E}_{\mathrm{c}}^{[j_1,j_1']}(\rho) \circ \mathcal{E}_{\mathrm{c}}^{[j_2,j_2']}(\rho) \circ \cdots \circ \mathcal{E}_{\mathrm{c}}^{[j_{N_2},j_{N_2}']}(\rho), \qquad (19)$$

with

$$\mathcal{E}_{\mathrm{c}}^{[j,j']}(\rho) = (1 - p_c)\rho + p_c X_j X_{j'} \rho X_{j'} X_j, \qquad (20)$$

where p_c is the probability of a single crosstalk error for $[j, j'] \in J'$, which leads to a correlated two-qubit bit-flip error. The error probability p_c can be expressed as

$$p_{\mathrm{c}} = \sin^2 C_{[j,j']}. \qquad (21)$$

For example, in the first parallel syndrome measurement, the parallel gate group shadowed by blue, which consists of three MS gates in Fig. 5(a), introduces 12 crosstalk terms shown in Fig. 2. It is clear from this perspective that the entangling crosstalk error model should be carefully considered in the context of the parallel FT circuit design, as a single MS gate error can turn into a dangerous pair of errors because some ions in J' belong to the set of physical data qubits.

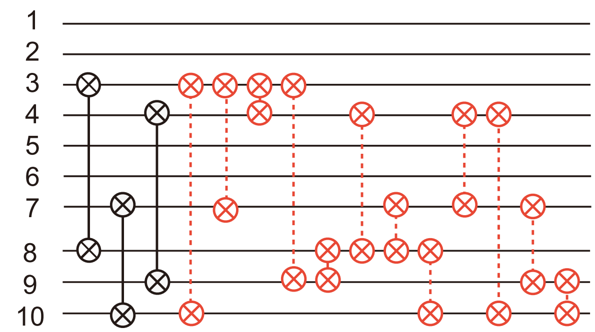

FIG. 2. The circuit representation of 12 crosstalk terms for the parallel gate group in the first parallel syndrome measurement. The MS gates in black represent the parallel gate group and the red dotted lines represent crosstalk terms.

III. FAULT-TOLERANT ERROR-CORRECTION CYCLE

A. Steane code

In this section, we focus on the $[7, 1, 3]$ stabilizer code [4,63], commonly referred to as the Steane code as depicted in Fig. 3(a), which is the smallest representative of the family of topological color codes. As a $[7, 1, 3]$ code, it encodes $n = 7$ physical qubits into a single logical qubit with logical distance $d = 3$, which allows one to detect and correct at least $t = 1$ arbitrary Pauli error on any of the seven physical data qubits. In addition to the locality property and high-FT threshold values, this code has another advantage that the entire group of Clifford gate operations can be implemented transversally [64], which is very beneficial for parallelism, as shown in Figs. 3(b) and 3(c). Besides, a universal set of logical gate operations can be achieved by complementing the Clifford operations with a single non-Clifford gate, such as the T gate by magic state injection [65,66].

As stated above, this code can independently detect and correct single-qubit bit- and phase-flip errors. These errors are detected by measuring a commuting set of weight-four Pauli operators known as stabilizers generators in Fig. 3(a):

$$\begin{aligned} S_X^{(1)} &= X_4X_5X_6X_7, \quad & S_Z^{(1)} &= Z_4Z_5Z_6Z_7, \\ S_X^{(2)} &= X_2X_3X_6X_7, \quad & S_Z^{(2)} &= Z_2Z_3Z_6Z_7, \\ S_X^{(3)} &= X_1X_3X_5X_7, \quad & S_Z^{(3)} &= Z_1Z_3Z_5Z_7. \end{aligned} \qquad (22)$$

Logical states are encoded in the joint simultaneous eigenspace of eigenvalue $+1$ of all six stabilizer generators, which are symmetric under exchange of X and Z.

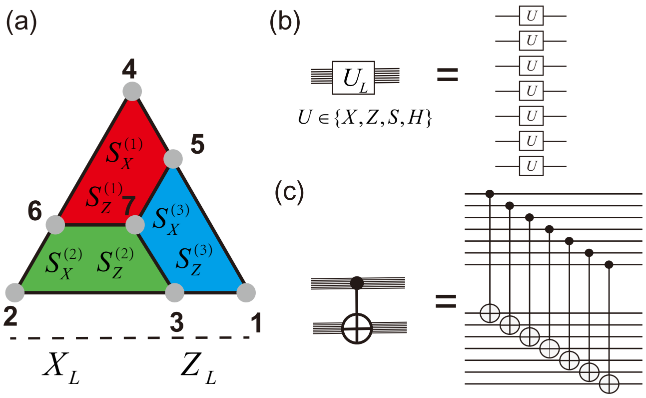

FIG. 3. Steane code. (a) We encode one logical qubit in $n = 7$ physical qubits, which can correct up to $t = 1$ arbitrary fault. Physical qubits are represented by the dots, which sit on the vertices of the graph. The six stabilizers in Eq. (22) correspond to the plaquettes that involves four data qubits of the 2D triangular color code structure. The logical operators X_L and Z_L act on the edge of the triangle. (b),(c) The transversal logical gates. All gates of the Clifford group can be implemented transversally and thus fault tolerantly. We note that we place over L subscripts on logical qubit operators and states to distinguish them from physical qubit operators and states.

B. QEC cycle

In this part, we discuss a parallel QEC protocol demonstrating a single logical qubit necessary for universal quantum computation in Figs. 1 and 4. We simulate individual rounds that begin with a FT logical state preparation, followed by a round of the syndrome extraction protocol in which we measure the stabilizers in parallel. We then apply a recovery operation based on the syndrome information from the stabilizer measurements using lookup tables. Finally, we measure all the data qubits to check if the protocol ended in success or failure.

Note that both sets of stabilizers follow from the definitions given in Fig. 3(a) and Eq. (22), but we use the f superscript to indicate syndromes measured using flagged circuits instead of those measured with unflagged circuits. For the simulations, we compile the circuits into MS gates to adapt them for the trapped-ion universal gate sets (see Appendixes B and D for details). In our scheme, the quantum circuit of every block is divided into several layers by black dotted lines, which represents that the quantum operations in the same layer are simultaneously executed, see Fig. 5 as an example. Considering the different operation time of each operation, every layer contains only the same type of operation.

1. Logical state preparation

The first pivotal QEC operation is the redundant encoding of a particular logical state [23,38,67], such as $|0\rangle_L$ as the $+1$ eigenstate of the logical Z operator Z_L. Instead of the postselection method, we adopt another protocol for deterministic FT Pauli state preparation in Fig. 4(a), which relies on the combination of the flag measurement and additional measurements of the logical operators $Z'_L = Z_1Z_4Z_5$ and $Z''_L = Z_2Z_4Z_6$ [38,67]. It should be noted we can proceed by rotating $|0\rangle_L$ to another logical Pauli basis state by applying the logical X_L, H_L, and S_L operators. To show the advantage of parallelism in QEC, we optimally divide the quantum gates into several parallel gate groups to decrease the circuit depth, especially for the second part, which simultaneously measures Z'_L and Z''_L. The details of the preparation of FT state and parallel quantum circuit are shown in Appendix B.

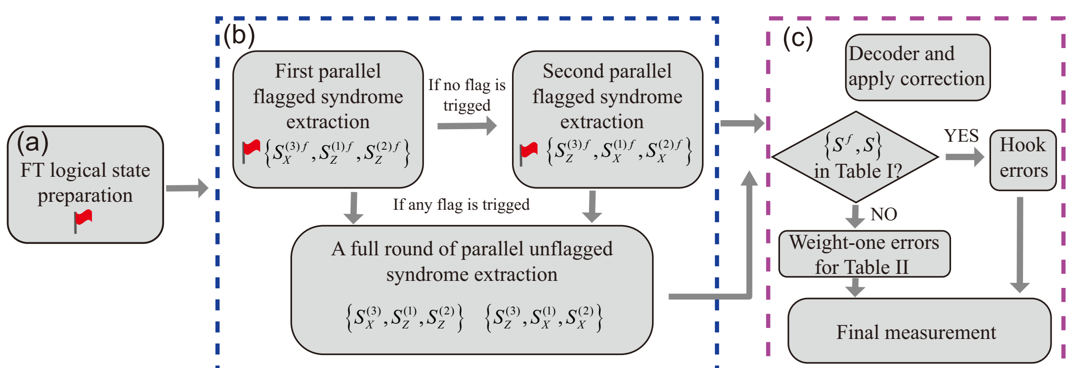

FIG. 4. QEC protocol. (a) The FT preparation of a logical basis state. (b) The parallel syndrome extraction protocol. We measure the first parallel flagged syndrome extraction of the stabilizers $\{S_X^{(3)f}, S_Z^{(1)f}, S_Z^{(2)f}\}$. If no flag is raised, we proceed to measure the second set of stabilizers $\{S_Z^{(3)f}, S_X^{(1)f}, S_X^{(2)f}\}$ using the flag scheme. If any flag was triggered, we do a second round of readouts in parallel without flags, $\{S_X^{(3)}, S_Z^{(1)}, S_Z^{(2)}\}$ and $\{S_Z^{(3)}, S_X^{(1)}, S_X^{(2)}\}$. If every flagged circuits does not indicate an error, the syndrome extraction completes. (c) Based on the information from the stabilizer measurements, we apply correction using the decoders. Finally, we measure all the data qubits to check if a logical error has happened.

2. Syndrome extraction protocol

One of the crucial operations in QEC is the readout of the stabilizer operators using ancillary qubits without affecting the quantum information encoded in the data qubits [21]. The syndrome extraction protocol operates by detecting changes in stabilizer measurement outcomes that ideally give $+1$ eigenvalue. However, the standard stabilizer measurement, which use a single ancillary qubit is not naively FT [36]. For example, a single fault on the ancillary qubit, which is called "hook errors" [37] can propagate through the CNOT gates and result in a weight-two fault on the data qubits that can lead to logical errors. To avoid a non-FT propagation of errors, various schemes have been developed to make the stabilizer readout FT [68–70].

In this work, we focus on a flag-based readout scheme [35–37] that one ancillary qubit as a syndrome qubit is used for the stabilizer measurement while a second ancillary qubit acts as a flag to indicate the possible occurrence of dangerous "hook errors." In previous works [38,71], the stabilizers in Eq. (22) are measured sequentially, we called this QEC cycle the serial scheme (see Appendix C). This syndrome extraction works slowly, which is a disadvantage in experiments with high idle error rates. Therefore, we adopt an alternative FT scheme [39] that allows extracting multiple syndromes in parallel as shown in Fig. 5, which we referred to as the parallel scheme. In this scheme, three stabilizers can be measured at once with only one extra qubit per stabilizer, with at the same time one syndrome qubit acting also as a flag to catch the "hook errors" while measuring another syndrome, shown in Fig. 5. This FT stabilizer measurement substantially reduces the number of required quantum gates, cutting down the depth of the circuit to lower the error probability of idle qubits.

To identify the "hook errors" from other weight-one errors, i.e., "nonhook errors" of similar syndrome signatures, the decoder requires two sets of syndrome measurements. Therefore, the syndrome extraction protocol consists of two parts as illustrated in Fig. 4(b). First, the flagged stabilizer syndromes $\{S_X^{(3)f}, S_Z^{(1)f}, S_Z^{(2)f}\}$ are measured using flagged parallel circuits shown in Fig. 5(a) in a way that identifies malignant "hook errors." If no flag is triggered, we proceed to the second set of three syndromes and measure the stabilizers $\{S_Z^{(3)f}, S_X^{(1)f}, S_X^{(2)f}\}$ using parallel flagged readout. If any flag was raised during every set of syndromes and a fault was detected, we realize a second full round of stabilizer readout without flags to distinguish "hook errors" from "nonhook errors," the first set being $\{S_X^{(3)}, S_Z^{(1)}, S_Z^{(2)}\}$ with parallel circuit design in Fig. 5(b) and the second set being $\{S_Z^{(3)}, S_X^{(1)}, S_X^{(2)}\}$.

Note that, in our work, the six stabilizers of the unflagged syndrome extraction can also be divided into two parallel sets $\{S_X^{(3)}, S_Z^{(1)}, S_Z^{(2)}\}$ and $\{S_Z^{(3)}, S_X^{(1)}, S_X^{(2)}\}$ as depicted in Fig. 5(b). Let us also remark that, for the unflagged syndrome measurements $\{S_X^{(3)}, S_Z^{(1)}, S_Z^{(2)}\}$, the parallel gate groups are slightly different from the flagged measurements $\{S_X^{(3)f}, S_Z^{(1)f}, S_Z^{(2)f}\}$. The MS-based quantum circuit for parallel syndrome extraction in Fig. 5 can be found in Appendix D. If no errors are indicated, the syndrome extraction protocol is complete. The combination of the flag readout with unflagged stabilizer measurements allows us to identify and correct the most likely error, preserving the FT character.

This scheme allows the simultaneous measurement of three stabilizers and then all six stabilizers can be measured in two rounds for the syndrome extraction of the Steane code. This tremendously reduces the cost of time to perform a QEC cycle during which idle qubits undergo decoherence. Whether in the parallel or serial FT protocol, the unflagged syndromes are treated as ideal measurements since they are measured only in the event that another error has been detected and the code is only guaranteed to correct a single error.

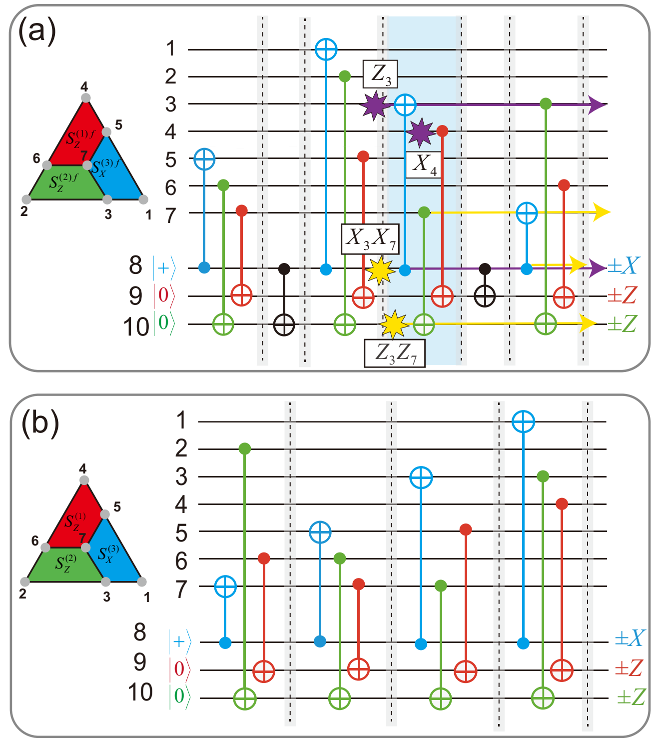

FIG. 5. (a) The first parallel flagged syndrome measurement $\{S_X^{(3)f}, S_Z^{(1)f}, S_Z^{(2)f}\}$. The blue CNOT gates extract the $S_X^{(3)f} = X_1X_3X_5X_7$ syndrome, while the red gates extract the $S_Z^{(1)f} = Z_4Z_5Z_6Z_7$ syndrome and the green gates extract the $S_Z^{(2)f} = Z_2Z_3Z_6Z_7$ syndrome. The black gates are there to catch bad faults, i.e., "hook errors." We mark fault locations with the eight-cornered stars that can trigger the measurement where the yellow stars represent the "hook errors" and the purple stars represent the "nonhook errors." The propagation paths for Z_3Z_7 and Z_3 faults are also shown in the circuit. The shaded blue part is the parallel gate group shown in Fig. 2. (b) The first parallel unflagged syndrome extraction of the stabilizers $\{S_X^{(3)}, S_Z^{(1)}, S_Z^{(2)}\}$.

TABLE I. Decoder for Z type “hook errors.”

$S_X^{(3)f}, S_Z^{(1)f}, S_Z^{(2)f}$	$S_X^{(1)}, S_X^{(2)}, S_X^{(3)}$	Correction
$-++$	$+-+$	Z_4Z_6
$--+$	$+-+$	Z_4Z_6
$-++$	$-++$	Z_3Z_7
$-+-$	$-++$	Z_3Z_7
$S_Z^{(3)f}, S_X^{(1)f}, S_X^{(2)f}$	$S_X^{(1)}, S_X^{(2)}, S_X^{(3)}$	Correction
$+--$	$-++$	Z_3Z_7
$---$	$-++$	Z_3Z_7

3. Decoder and measurement

At the end of a QEC cycle, the information of syndrome measurements are sent to the decoder, i.e., lookup table to infer a correction. In this part, we introduce only the Z errors of syndrome because of symmetry and the lookup tables for X errors can be found in Appendix E.

The first lookup table (see Table I) is concerned with “hook errors.” For single-qubit errors, “hook errors” can produce the same syndrome as other less damaging weight-one “nonhook errors.” As shown in Fig. 5(a),“hook error” is the single-Z error at the location marked Z_3Z_7, which will spread into weight-two error. As we can see, Z_3Z_7 and Z_3 is distinguishable in the first parallel flagged syndrome extraction of the stabilizers with $\{S_X^{(3)f}, S_Z^{(1)f}, S_Z^{(2)f}\} = [-,+,+]$. Therefore, we realize a second full round of six stabilizers readout without flags. If the syndromes of $\{S_X^{(1)}, S_X^{(2)}, S_X^{(3)}\}$ are $[-,+,+]$, the correction is Z_3Z_7 while Z_3 error occurs with $[+,-,-]$ measurements.

The second decoder (see Table II) utilizes the unflagged syndrome measurements $\{S_X^{(1)}, S_X^{(2)}, S_X^{(3)}\}$ and ignores the flagged syndrome measurements to correct the “nonhook errors.” Therefore, the corrections determined by Tables I and II give the final recovery operation for the current QEC cycle.

Finally, the state is measured to check if the protocol ended in success.

TABLE II. Decoder for weight-one “nonhook errors.” The correction is only based on the unflagged syndrome measurements.

$S_X^{(1)}, S_X^{(2)}, S_X^{(3)}$	Correction
$+++$	I
$++-$	Z_1
$+-+$	Z_2
$+--$	Z_3
$-++$	Z_4
$-+-$	Z_5
$--+$	Z_6
$---$	Z_7

IV. RESULTS OF QEC

For QEC to be helpful in FT computations, logical error rate must be lower than the physical error rate in the typical circuits and the crossover point is known as the FT threshold. In this section, we assess the performance of the parallel FT protocol compared to physical qubit operations to estimate break-even points of FT advantage. The logical fidelity F_L is determined by expectation value of logical Pauli operators P_t onto the respective axis $t \in \{X_L, Y_L, Z_L\}$ of the logical Bloch sphere

$$F_L = \frac{1}{2}\langle 1 \pm P_t\rangle. \tag{23}$$

The definition of the logical failure rate is the logical infidelity $\delta F_L = 1 - F_L$. In this work, we focus on the simulation of the logical state $|+\rangle_L$ as it is easily affected by the dephasing errors on idle qubits.

To estimate logical error rates of logical state preparation protocol, we perform numerical stabilizer simulations of stochastic incoherent Pauli noise models as described above. The stabilizer simulations can provide faster results that allow for a quick evaluation of the behavior of a given process compared to the state-vector simulations. All simulations in this work are performed using a modified version of the performance estimator of codes on surfaces (PECOS) package, which is a Python framework for studying and evaluating QEC protocols [72,73]. The effect of different incoherent noise models is treated by means of direct Monte Carlo sampling. Each data point in our figures is the averaged result of at least 10^7 runs.

A. Crosstalk threshold

Firstly, we independently study the influence of three incoherent noises, depolarizing noise on MS gates, crosstalk noise of parallel gates and optical addressing crosstalk noise, on the performance of Steane code in Fig. 6(a). As we can see, the logical error probability δF_L for MS gate error rate p_{MS} is quadratic at low physical error rate and the regime of advantageous FT implementation can then be found. As described in the text, quadratic scaling behavior is the signature of a correct FT circuit. However, the scaling of the logical error rate δF_L with crosstalk error rate p_c is linear, which shows crosstalk noise does not respect the FT property of the QEC cycle.

As depicted in Fig. 2, crosstalk fault operators can potentially propagate to cause uncorrectable weight-two errors on data qubits at the end of the circuit without triggering the flag. This illustrates that even though the logical failure rates of FT circuits are expected to scale quadratically, there exists a linear term in the expansion of δF_L caused by dangerous crosstalk errors which will eventually destroy the advantageous scaling behavior [shown in Fig. 6(a)]. At this point, it seems clear that the entangling

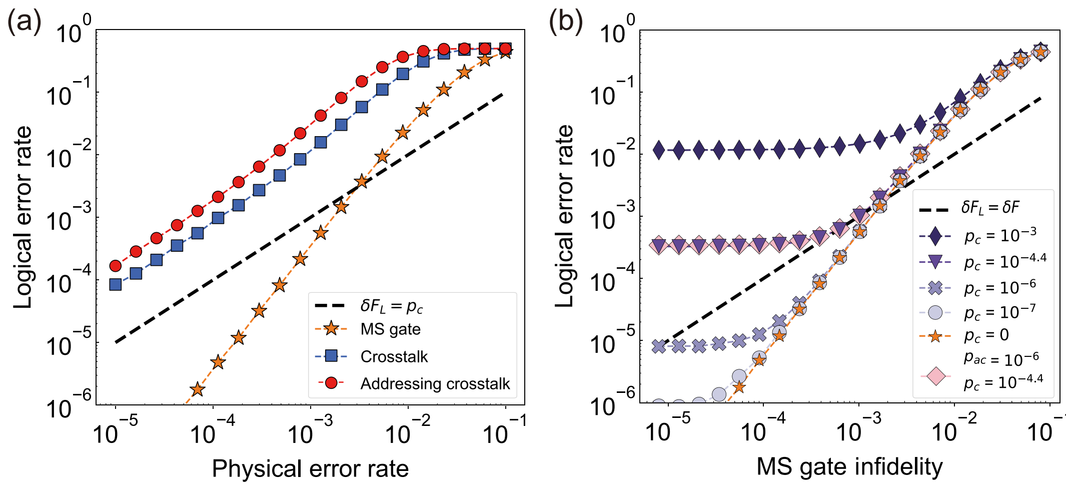

FIG. 6. (a) The logical error rates δF_L using a limited error model that includes the incoherent crosstalk error only (blue line with squares), the MS gate error only (orange line with stars), and the optical addressing crosstalk error (red line with circles). The black dashed line represents $\delta F_L = p_c$ and $\delta F_L = p_{\mathrm{MS}}$, which is used to find the break-even point of FT advantage. The noise model of the optical addressing crosstalk error is similar to that in Ref. [30]. (b) The logical error rates δF_L as a function of the MS gate infidelity δF for a fixed crosstalk error rate p_c. For each line, only the MS gate error rate varies and the crosstalk error rate is fixed. The black dashed line represents $\delta F_L = \delta F$. The pink line with squares represents the logical error rates δF_L for fixed crosstalk error rate $p_c = 10^{-4.4}$ and $p_{ac} = 10^{-6}$..

crosstalk error should be carefully considered in the context of the parallel FT circuit design, as a single crosstalk error can turn into a dangerous pair of errors when both ions of crosstalk pairs are physical data qubits. The optical addressing crosstalk noise shows the similar behavior as the crosstalk noise of parallel gates [shown in Fig. 6(a)]. If this noise is not adequately suppressed, it can break the fault tolerance of the QEC cycle as discussed in Ref. [30].

Therefore, we should identify a critical value of crosstalk errors below, which it is possible to reach the break-even point of quantum logical advantage. In general, the threshold estimate is difficult because it requires a detailed understanding of the system's underlying physics. One criterion is that the logical operation realized within a given hardware architecture should be compared to the corresponding physical operation as it could be realized in exactly that same hardware architecture suggested in Ref. [74]. However, in cases where the dominant physical noise mechanism is known, as done previously, e.g., in Refs. [62,71], one method is to scale the noise mechanism in simulations and define it as the break-even point where the logical error rate is equal to the dominant physical noise source.

As discussed previously for trapped-ion systems, the largest physical error is the noise of entangling MS gates. Here we opt to compare the logical error rate with the MS gate error rate and run simulations for different constant values of crosstalk error rate with varying depolarizing error rates. Our goal is to find a parameter range of MS gate infidelity, under which, again in the limit of a dominant error source, crosstalk error, FT retention of the encoded information would be possible. As can be seen in Fig. 6(b), we find that there exists an upper limit on crosstalk error rate $p_c = 10^{-4.4}$ to achieve fault tolerance with the entangling MS gate infidelity $\delta F = 1.86 \times 10^{-3}$. Within a range of physical entangling gate infidelity $\delta F = \{1.86 \times 10^{-3} \sim 10^{-5}\}$, which is realistic for current architecture, reducing the crosstalk error rate to a value on the order of $p_c = 10^{-6}$ might be appropriate for achieving FT of parallel quantum circuit design of a QEC cycle.

In addition, according to Ref. [30], the FT threshold of the Steane code can be obtained for an optical addressing crosstalk error rate not larger than p_{ac} of 10^{-6}, when the MS-gate error lies below $p_{\mathrm{MS}} = 2 \times 10^{-3}$. Recently, some experimental studies have reduced the optical addressing crosstalk error rate to the $p_{ac} = 10^{-6}$ level [32–34]. Therefore, we consider a situation in which the depolarizing error rate varies with a fixed crosstalk error rate of $p_c = 10^{-4.4}$ and a fixed optical addressing crosstalk error rate of $p_{ac} = 10^{-6}$. As can be seen in Fig. 6(b), the line of logical error rate for $p_c = 10^{-4.4}$ and $p_{ac} = 10^{-6}$ coincides with the line of logical error rate for $p_c = 10^{-4.4}$. It implies that the crosstalk noise of parallel gates becomes a dominant error source when the optical addressing crosstalk is effectively suppressed under the current experiment condition.

Let us also remark that, as the MS gate infidelity decreases, the lines of logical infidelity become plateaulike leveling. This is because, if the MS gate infidelity is reduced well below the levels of crosstalk error, the crosstalk error will be the leading ones of the logical error rate. The plateaulike effects observed on the logical

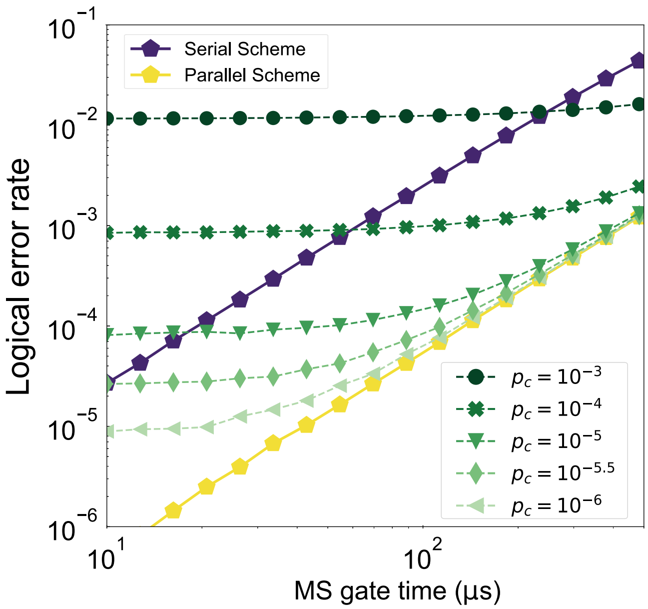

FIG. 7. The logical error rates δF_L of the parallel scheme as a function of the operation time of MS gate τ under the influence of varying dephasing error rates and constant crosstalk error rate. The yellow (bark purple) line with pentagon markers represents the logical error rate with limited the error model to dephasing error only of the parallel (serial) scheme.

error rate depend on the fixed values of crosstalk fault. Although crosstalk noise still has the ability to destroy FT in the Steane code, it is no longer a limiting factor for QEC performance in experimentally relevant regions when suppressed below the FT threshold.

B. The advantage of parallelism

Typically, environmental dephasing is considered to be the main source of noise affecting idle trapped-ion qubits. As shown in Fig. 7, when limiting the error model to dephasing errors only, the logical infidelity of the serial scheme is much higher than the parallel scheme. This implies that if qubits accumulate errors rapidly at rest, it is useful to extract multiple MS gates in parallel, which can provide significant improvement in the execution time of the entire circuit and dramatically decrease the error probability of idle qubits.

However, parallel gates will introduce damaging crosstalk errors as a single crosstalk fault can lead to a noncorrectable error. Therefore, we also show the logical infidelity under the influence of varying dephasing error rates and a constant crosstalk error rate in Fig. 7. In the experimentally accessible regime, we choose the time of operations, single-qubit gate, two-qubit MS gate, qubit reset and measurement, are $\{0.05\tau, \tau, \tau, 1.5\tau\}$ where τ is the MS gate time. And then we can get the error probability of each idle qubit in Eq. (15) by dividing the quantum circuit into several layers. Among the MS gate time in the range of $\tau \in [10, 500]$ μs, the crosstalk error rate should be reduced to $p_c = 10^{-5.5}$ and below that, the logical error rate of parallel scheme is lower than the serial scheme, which displays the advantage of parallelism.

Overall, to demonstrate FT quantum logical advantage over physical qubits and effectiveness of the parallelism for QEC protocol, it is sufficient to lower the crosstalk error rate p_c below the FT threshold $p^{\text{thres}} = 10^{-6}$ and the infidelity of MS gate δF below $\delta F^{\text{thres}} = 1.86 \times 10^{-3}$, which are still conservative for the current parallel QEC cycle of the logical qubit. According to the definition of the crosstalk error rate in Eq. (21), the crosstalk $C_{[j,j']}$, i.e., the entangling phase for pair $[j, j'] \in J'$ should be lower than the threshold $C^{\text{thres}} = 10^{-3}$. Depending on the QEC codes and the noise models, there exist different FT thresholds. Here, we have derived the FT thresholds for the crosstalk error and the MS gate infidelity specially for the Steane code.

V. PARALLEL GATES WITH AN OPTICAL TWEEZER ARRAY

As we have seen in the previous section, crosstalk errors can cause a damaging effect on a logical qubit's QEC performance and should be mitigated below the FT threshold. Here, we propose an effective protocol for programming the array of optical tweezers to attain a set of localized modes and gapped mode frequencies and designing high-fidelity, low-crosstalk parallel two-qubit gates in the quantum circuit of a QEC cycle.

A. Localized modes of an optical tweezer array

Optical tweezers allow a site-dependent manipulation of the trapping or antitrapping optical potential through the ac Stark effect experienced by internal energy states of ions [43–46]. For a Gaussian optical tweezer propagating along the y dirction as illustrated in Fig. 8(a), the optical dipole potential can be approximated as harmonic in the vicinity of the focuses of the tweezers. In this work, we assume the state dependence of optical potential to be negligible and the optical trapping frequency along the beam axis y compared to other axis is negligible [47]. The transverse motional modes and the corresponding frequencies of ion chain with an optical tweezer array can be precisely calculated; see Appendix F for details.

To be specific, we consider a chain of 12 ions with one buffer ion at each edge and use the central ten ions to implement parallel entangling gates. To achieve an average spacing of $d = 10$ μm, we choose the trapping frequency $\omega_x = \omega_y = 2\pi \times 2.049$ MHz and $\omega_z = 2\pi \times 0.0638$ MHz. The MS gates of parallel gate group in our work are performed on pinned ion pairs with optical tweezers. We consider a situation in which the tweezer

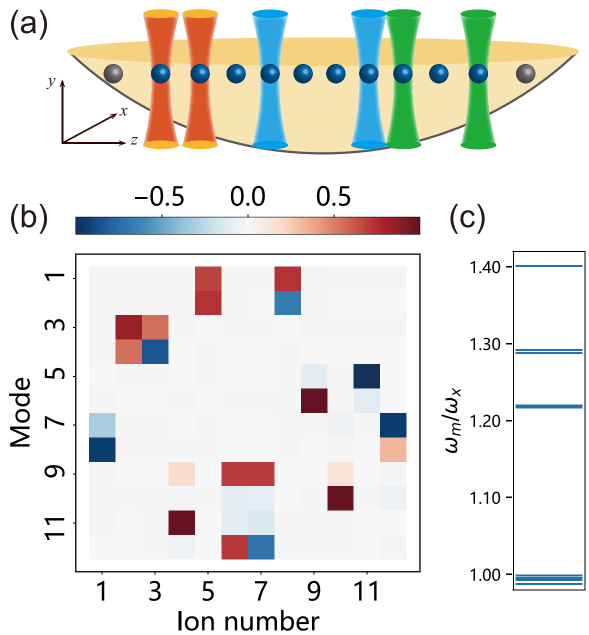

FIG. 8. (a) The $N = 12$ ion chain in an array of optical tweezers along the y direction. The parallel three entangling gates with tweezers are performed on ion pairs $[2,3], [5,8]$, and $[9,11]$. The first and last buffer ions (gray dots) are not used as qubits. (b) The x transverse motional modes b_j^m, $j, m = 1, \ldots, 12$ with programmable tweezer array $\{\omega^{\mathrm{tw}}_{[2,3]}, \omega^{\mathrm{tw}}_{[5,8]}, \omega^{\mathrm{tw}}_{[9,11]}\} = \{0.821\omega_x, 0.989\omega_x, 0.703\omega_x\}$. The oscillation amplitude and direction of ions are represented by the color of the squares. (c) The mode frequency spectrum ω_m/ω_x is shown on the right side. The difference of two frequencies in the first set is vanishingly small on the scale of the figure. The order of mode in (b) reflects the mode frequency, with the first mode corresponding to the highest frequency.

intensity of each ion pair is different, whereas the remaining ions are not pinned and two ions in an MS gate have the same tweezer strength. Then the programmable optical tweezer array can then be expressed as $\omega^{\mathrm{tw}} = \{\omega^{\mathrm{tw}}_{[j_1,j'_1]}, \omega^{\mathrm{tw}}_{[j_2,j'_2]}, \ldots, \omega^{\mathrm{tw}}_{[j_{N_1},j'_{N_1}]}\}$ where $\omega^{\mathrm{tw}}_{[j_{N_1},j'_{N_1}]}$ is the optical trapping frequency and N_1 is the number of MS gates in a parallel gate group. In this section, we present the motional modes b_j^m and mode frequencies ω_m of parallel entangling ion pairs $[2,3], [5,8]$, and $[9,11]$ with different optical tweezer intensities $\{\omega^{\mathrm{tw}}_{[2,3]}, \omega^{\mathrm{tw}}_{[5,8]}, \omega^{\mathrm{tw}}_{[9,11]}\} = \{0.821\omega_x, 0.989\omega_x, 0.703\omega_x\}$ as illustrated in Fig. 8(a). As shown in Figs. 8(b) and 8(c), the transverse modes and the corresponding frequencies in the presence of tweezers drastically differ from those for the ion chain without tweezers.

One of the key features is that the motion of pinned ions is almost completely decoupled from that of ions, which is not illuminated by an optical tweezer. Of note, each ion pair with different tweezer intensity is mutually independent. The motional modes of each pair are localized, which consists only of center of mass (COM) and stretch modes where the pinned ions dominant motion. In other words, the modes, which are localized on a pair of pinned ions, have almost zero amplitudes on ions that belong to another ion pair with different tweezer intensity. In fact, the crosstalk between ion pairs of parallel gates is related to the collective motional modes in which all ions have nonzero oscillation amplitudes. This unwanted effect can be strongly suppressed if the difference between the squares of the local oscillation frequencies of the pinned ions in different ion pairs, is large in comparison to their residual Coulomb interaction. Note that when all ions are pinned with the same optical-trapping frequency, their localized modes hybridize, which is in principle unfavorable for reducing crosstalk as detailed in Appendix F. Therefore, these localized modes based on an optical tweezer array with different intensities are the desired modes to implement parallel high-quality two-qubit entangling gates.

As illustrated in Fig. 8(c), the mode frequencies of the ion chain in the optical tweezer array are gapped and split up into several subsets. The three subsets appearing shifted above corresponds to the localized modes of three ion pairs illuminated by optical tweezers. Each subset consists of two mode frequencies, the COM frequency ω^{COM} and stretch frequency $\omega^{\mathrm{stretch}}$, where the frequency splitting is determined by the Coulomb interaction. In this work, we aim at implementing the ith MS gate of parallel group with the detuning $\mu_{[j_i,j'_i]}$ in the neighborhood of the $\omega^{\mathrm{COM}}_{[j_i,j'_i]}$ or $\omega^{\mathrm{stretch}}_{[j_i,j'_i]}$, where $i = 1, 2, \ldots, N_1$ in Fig. 8(c).

These features of localized motional modes and gapped frequencies can be improved by either increasing the tweezer-trapping frequency or by increasing the spacing of the ions. By dynamically reconfiguring the tweezer array, the designer motional modes can be adjusted during running quantum computations, and thus offer great flexibility to achieve a different parallel gate group of the FT circuit.

B. Numerical optimization scheme

Our protocol of the realization of high-quality parallel gates relies on finding the satisfied confinement realized by the tweezer at the position of each ion pair. We solve this problem through two optimization steps.

1. Presearch technique: LD parameter

The first step of the optimization approach focuses on the localized motional modes and the gapped mode frequencies, which is related to LD parameters. As described in Eqs. (3) and (12), the crosstalk of ion pairs J' is influenced by LD parameters $\eta_j^m \eta_{j'}^m$, where $[j, j'] \in J'$. When we manipulate the tweezers to make the motional modes of each pair more localized, the LD terms can be decreased greatly, and then crosstalk can be effectively suppressed. In addition, the gate infidelity can be obviously decreased with only a few pulse segments when the mode vectors of every pair excluded the localized COM and stretch modes have almost zero amplitudes, i.e., $|\eta_j^m|^2 + |\eta_{j'}^m|^2$, according to Eqs. (2) and (11). In this way, we can find an approximation to the optimal tweezer array by optimizing the values of LD parameters, without having to solve numerically the pulse shape.

The first step takes the following parameters as inputs: the number of ions N, the ion pairs in the presence of tweezers J. The arguments are the optical trapping intensity of tweezers, $\omega^{\mathrm{tw}} = \{\omega^{\mathrm{tw}}_{[j_1,j_1']}, \omega^{\mathrm{tw}}_{[j_2,j_2']}, \ldots, \omega^{\mathrm{tw}}_{[j_{N_1},j_{N_1}']}\}$.

The LD parameter term of crosstalk can be expressed as

$$F_c^{\mathrm{LD}}(\omega^{\mathrm{tw}}) = \frac{1}{N_2}\sum_{[j_i,j_i']}\sum_m \left|\eta_{j_i}^m \eta_{j_i'}^m\right|, \tag{24}$$

where $[j_i,j_i'] \in J'$ for $i = 1,2,\ldots,N_2$.

The LD parameter term of gate infidelity can be described as

$$F_{if}^{\mathrm{LD}}(\omega^{\mathrm{tw}}) = \frac{1}{N_1}\sum_{[j_i,j_i']}\sum_{m'}\left(\left|\eta_{j_i}^{m'}\right|^2 + \left|\eta_{j_i'}^{m'}\right|^2\right), \tag{25}$$

where $[j_i,j_i'] \in J$ for $i = 1,2,\ldots,N_1$ and the summation over m' are limited to N_2 motional modes, which exclude their localized COM and stretch modes.

This problem is formulated as mulitobject optimization problem with constraints of the form:

$$\begin{aligned} &\min_{\omega^{\mathrm{tw}}} \mathbf{F}^{\mathrm{LD}}(\omega^{\mathrm{tw}}) = [F_c^{\mathrm{LD}}(\omega^{\mathrm{tw}}), F_{if}^{\mathrm{LD}}(\omega^{\mathrm{tw}})]^T \\ &\text{s.t. } \omega^{\min} \le \omega^{\mathrm{tw}}_{[j_i,j_i']} \le \omega^{\max}, \quad i = 1,\ldots,N_1, \end{aligned} \tag{26}$$

where $\mathbf{F}^{\mathrm{LD}}(\omega^{\mathrm{tw}})$ is a vector of objective functions. The feasible design space is defined as $\omega^{\mathrm{tw}} = \{\omega^{\min} \le \omega^{\mathrm{tw}}_{[j_i,j_i']} \le \omega^{\max}, i = 1,\ldots,N_1\}$, where $\omega^{\max}$ and $\omega^{\min}$ are maximum and minimum of the tweezer intensity, respectively.

In this work, we use the weighted-sum method [75] to solve the problem in Eq. (26) with scalar weights w_i and minimize the following composite objective function:

$$\begin{aligned} &\min_{\omega^{\mathrm{tw}}} F^{\mathrm{LD}}(\omega^{\mathrm{tw}}) = w_1 F_c^{\mathrm{LD}}(\omega^{\mathrm{tw}}) + w_2 F_{if}^{\mathrm{LD}}(\omega^{\mathrm{tw}}) \\ &\quad \text{s.t. } \omega^{\min} \le \omega^{\mathrm{tw}}_{[j_i,j_i']} \le \omega^{\max}, \quad i = 1,\ldots,N_1. \end{aligned} \tag{27}$$

The weights satisfy $w_1 + w_2 = 1$ and are determined by the crosstalk threshold C^{thres} and infidelity threshold $\delta F^{\mathrm{thres}}$. The linear weighted-sum method makes the multiobjective function into a single-objective optimization problem.

Due to the nonconvex property of target function, there exist many local extreme points. These local extreme points can greatly decrease the LD parameter terms in Eq. (27) and then suppress the crosstalk and improve gate fidelity. Therefore, this optimization step can be regarded as a presearch technique, which can improve the search efficiency and provide many good initial guesses to the second nonlinear optimization problem.

2. Optimization: the exact target function

We optimize the precise values of crosstalk and gate infidelity in a second step to below the FT threshold by considering the parallel gate parameters, such as the set of detunings $\mu = \{\mu_{[j_1,j_1']}, \mu_{[j_2,j_2']}, \ldots, \mu_{[j_{N_1},j_{N_1}']}\}$, gate times $\tau = \{\tau_{[j_1,j_1']}, \tau_{[j_2,j_2']}, \ldots, \tau_{[j_{N_1},j_{N_1}']}\}$, the pulse segments $N_{\mathrm{seg}} = \{N_{\mathrm{seg}}^{[j_1,j_1']}, N_{\mathrm{seg}}^{[j_2,j_2']}, \ldots, N_{\mathrm{seg}}^{[j_{N_1},j_{N_1}']}\}$ and the pulse shape of each MS gate $\mathbf{\Omega}^{[j_i,j_i']}$ for $i = 1,2,\ldots,N_1$ where $\mu_{[j_i,j_i']}$, $\tau_{[j_i,j_i']}$ and $N_{\mathrm{seg}}^{[j_i,j_i']}$ is the given parameter of i-th ion pair of parallel gate group J. In this optimization part, the sequence of Rabi frequencies of ith ion pair $\mathbf{\Omega}^{[j_i,j_i']}$ under the parameters $\mu_{[j_i,j_i']}$, $\tau_{[j_i,j_i']}$, and $N_{\mathrm{seg}}^{[j_i,j_i']}$ is determined by the approach in Appendix A.

In the section about QEC, we assume that the error probability p_c of each ion pair $[j,j'] \in J'$ is the same. Therefore, to achieve the FT advantage of QEC, we should guarantee the maximum value of crosstalk and infidelity terms of each parallel gate group below the FT threshold for conservative estimates. Based on Eq. (12), the objective function of crosstalk can be expressed as

$$F_c = \max[|C_{[j_1,j_1']}|, |C_{[j_2,j_2']}|, \ldots, |C_{[j_{N_2},j_{N_2}']}|], \tag{28}$$

where $[j_i,j_i'] \in J'$ for $i = 1,2,\ldots,N_2$.

The objective function of gate infidelity can be described as

$$F_{if} = \max[\delta F_{[j_1,j_1']}, \delta F_{[j_2,j_2']}, \ldots, \delta F_{[j_{N_1},j_{N_1}']}], \tag{29}$$

where $[j_i,j_i'] \in J$ for $i = 1,2,\ldots,N_1$.

Therefore, the target function in the combination of crosstalk and gate infidelity using weights can be expressed as

$$\begin{aligned} &\min_{\omega^{\mathrm{tw}}} F(\omega^{\mathrm{tw}}) = w_1 F_c(\omega^{\mathrm{tw}}) + w_2 F_{if}(\omega^{\mathrm{tw}}) \\ &\text{s.t. } \omega^{\min} \le \omega^{\mathrm{tw}}_{[j_i,j_i']} \le \omega^{\max}, i = 1,\ldots,N_1. \end{aligned} \tag{30}$$

We perform a second search using the local extreme points found in the presearch technique as the initial guess. For the results presented in this work, we have used a pseudo-Hessian method (L-BFGS-B) [76] to perform the optimizations of Eqs. (27) and (30). In the numerical optimization

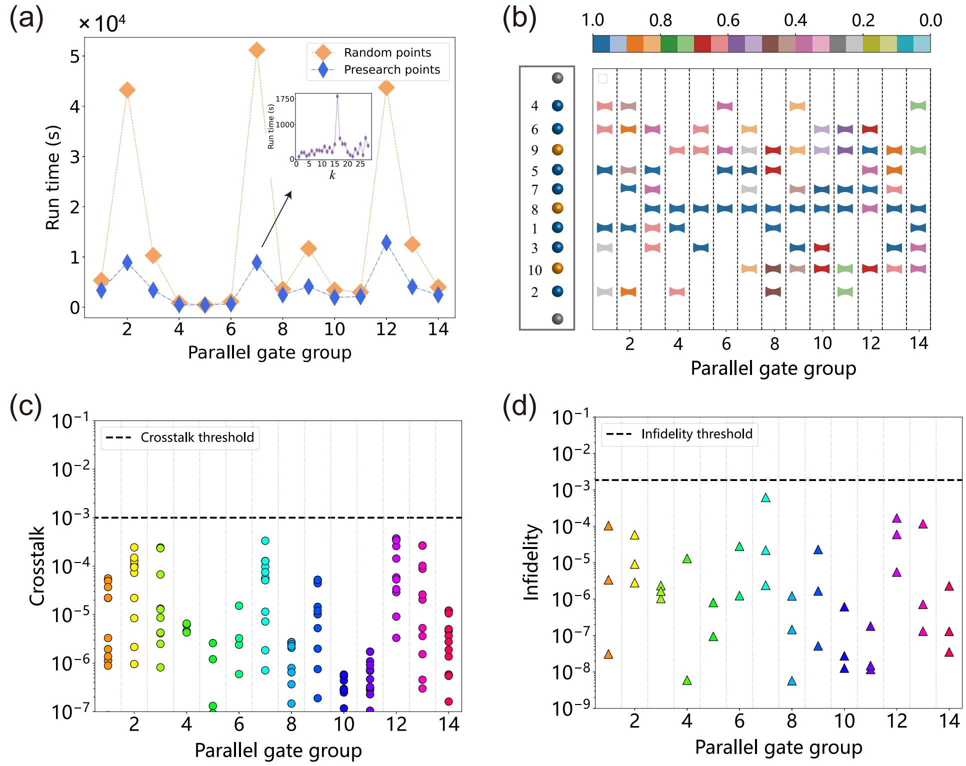

FIG. 9. (a) The run time of each parallel gate group used in the QEC circuit. The blue rhombuses represent the sum run time of a set of detunings for our optimization method based on an efficient presearch technique. The orange diamonds represent the run time of the optimization method based on a random initial guess. The inset plots the run time of different detuning of the rhombus, highlighted by the black arrow for the parallel gate group $\{[3,10],[4,6],[5,7]\}$. The set of detunings of each group are in the vicinity of the corresponding localized modes where the kth element can be expressed as $\{\mu_{[j_1,j_1']},\mu_{[j_2,j_2']},\ldots,\mu_{[j_{N_1},j_{N_1}']}\}_k=\{\omega^{\text{stretch}}_{[j_1,j_1']}+(-1+3k/28)(\omega^{\text{COM}}_{[j_1,j_1']}-\omega^{\text{stretch}}_{[j_1,j_1']}),\omega^{\text{stretch}}_{[j_2,j_2']}+(-1+3k/28)(\omega^{\text{COM}}_{[j_2,j_2']}-\omega^{\text{stretch}}_{[j_2,j_2']}),\ldots,\omega^{\text{stretch}}_{N_1}+(-1+3k/28)(\omega^{\text{COM}}_{[j_{N_1},j_{N_1}']}-\omega^{\text{stretch}}_{[j_{N_1},j_{N_1}']})\}$, where N_1 is the number of MS gates in group and $k=\{0,1,\ldots,28\}$. Every two-qubit gate in each parallel gate group is demonstrated with the pulse segments $N_{\text{seg}}=5$ and the gate duration $\tau=200\,\mu\text{s}$. (b) The optimized results of the optical tweezer array for a different parallel layer as indicated in every column. The color of labels represents the intensity of tweezer. The ion-qubit mapping is shown in the left part where the order of the qubits used for FT QEC in the ion string is labeled by the number beside the circles. Data qubits are depicted in blue and ancillary qubits are labeled orange. (c) The crosstalk values of parallel gate groups with the optimized tweezer array as shown in (b). Every column displays the crosstalk values of each parallel gate group. The dashed black line represents the crosstalk threshold. (d) The infidelity of MS gates as a function of parallel gate groups. The dashed black line represents the infidelity threshold.

scheme of our work, the second optimization process will stop once a satisfied tweezer array has been found. A satisfied tweezer array means that, based on this tweezer array, the performance of parallel gates meets the demand of the crosstalk and the gate infidelity below the FT threshold. On the basis of the initial guess, the optimization of Eq. (30) quickly converges and significantly saves the computing resources.

VI. RESULTS OF PARALLEL GATES

In this section, we investigate the performance of the FT protocol with parallel two-qubit quantum gates under depolarizing noise on MS gates, dephasing noise on idling qubits and crosstalk error of parallel two-qubit gates. We find that it is sufficient to lower the crosstalk $C_{[j,j']}$ for pair $[j,j']\in J'$ than $C^{\text{thres}}=10^{-3}$ and the infidelity of MS gate $\delta F_{[j,j']}$ for $[j,j']\in J$ than 1.86×10^{-3}. As stated above, the FT threshold depends on the choice of QEC code and the nature of the noise in the physical qubit. Note that the FT thresholds for the crosstalk error and the MS gate infidelity in this work are specific for the logical qubits protected by the Steane code. For other QEC codes, the FT threshold may be different. For the QEC cycle of a logical qubit based on Steane code, there exist 14 kinds of parallel gate groups in the FT quantum circuit where the FT logical state preparation has six types and the syndrome extraction protocol has eight, respectively. As illustrated in Fig. 5(a), there exist four groups of parallel MS gates.

Here, we provide the results of efficient optimization protocol, which can find satisfied optical tweezer strengths for 14 parallel gate groups that are required to decrease the maximum value of crosstalk and infidelity terms of each parallel gate group below the FT threshold in a linear chain of 12 $^{171}\mathrm{Yb}^+$ ions. We consider one ion string ordering [in Fig. 9(b)], in which ions in positions 7, 4, and 10 correspond to the ancillary qubits and other ions correspond to qubits 1–7 of the Steane code based on the local property of the stablizers. We assume that $\omega^{\mathrm{tw}}_{[j_i j_i']}$ can take on values up to $\omega^{\max} = 0.99\omega_x$ for typical transverse trapping frequencies and $\omega^{\min} = 0$ for $i = 1, 2, \ldots, N_1$.

To show the search effectiveness of our optimization method, we evaluate the search performance using the sum of run time for a set of detunings and compare the results of 14 parallel gate groups with those of other random initial guess. As shown in Fig. 9(a), starting points based on the pre-search technique can improve the search efficiency greatly and quickly converge to a satisfied solution compared to arbitrary starting points.

We also demonstrate the availability of our optimization scheme by an example with all MS gates with the same pulse segments $N_{\mathrm{seg}} = 5$ and the gate duration $\tau = 200\,\mu\mathrm{s}$. The detunings of each parallel gate group are in the vicinity of corresponding localized mode frequencies with $\{\mu_{[j_i j_i']} = 2\omega^{\mathrm{stretch}}_{[j_i j_i']} - \omega^{\mathrm{COM}}_{[j_i j_i']}\}$ for $i = 1, 2, \ldots, N_1$ where N_1 is the number of MS gates in the group. The optimized optical tweezer arrays for a different parallel layer are indicated in every column of Fig. 9(b). We notice that the intensity of the optimized tweezer array is mostly concentrated in high strength, which makes the modes of every pinned pair more localized. As we can see in Figs. 9(c) and 9(d), the values of crosstalk terms for each parallel gate group with an optimized tweezer array all can be reduced below the FT threshold. The infidelity of MS gates can also be decreased below $\delta F^{\mathrm{thres}}$ using only $N_{\mathrm{seg}} = 5$ pulse segments, which indicates that the localized modes are desired modes to implement high-fidelity two-qubit entangling gates.

So far, our discussion mainly focused on a linear ion chain. To further scale up the ion number, one promising scheme is to trap the ions in a two-dimensional crystal [34,77–79] in addition to the quantum charge-coupled device (QCCD) and an ion-photon quantum network. Here, we extend the scheme to a two-dimensional ion crystal confined by a Paul trap, which is a remarkable way to achieving a scalable quantum computation and quantum simulation [34].

In terms of the QEC cycle, we can naturally choose the hexagonal plaquette of the two-dimensional ion crystal to encode the Steane code due to the planer structure for the ion-qubit mapping. In terms of the parallel gates, there exists a noticeable micromotion problem for two-dimensional ion crystal compared to a linear ion chain [34,80,81]. The fast micromotion problem on the equilibrium ion position is caused by strong fast-oscillating electric field. Some theoretical studies [80,81] showed that the micromotion can be considered in the design of the quantum gates and does not significantly affect the entangling gates. Recently, the authors in Ref. [34] demonstrated that the effect of micromotion can be compensated by a recalibration of the laser intensity without degrading the gate fidelity in experiments.

Therefore, in terms of the parallel gates based on the programmable optical tweezer array, we can also consider the micromotion effect in the optimization of the quantum gates, as discussed in Ref. [34,80,82]. When we consider the in-plane micromotion and out-of-plane modes, the localized motional modes and gapped mode frequencies are slightly modified due to the micromotion, following the procedure described in Ref. [83]. In the design of the quantum gates in Sec. V, the addressing laser profile seen by the ion is time dependent due to the in-plane micromotion, which causes the amplitude modulation in the addressing beam [80]. In addition to the individual addressing technique in the two-dimensional ion crystal [34], the addressing of the optical tweezer beam is an experimental challenge at the moment. However, these experimental challenges would be attempted with the fast advances of relevant technologies [83]. Combined with the addressing technique of individual ions in two-dimensional ion crystal, our high-quality parallel gates are promising for a powerful tool for the large-scale fault-tolerant quantum computation within a single Paul trap.

VII. CONCLUSIONS AND OUTLOOK

The demonstration of a QEC cycle restricted to a single logical qubit is one of the promising paradigms to reach the break-even point where FT circuits will outperform physical qubits. In this work, we have provided a detailed numerical study and analysis of the crosstalk errors of parallel gates on QEC performance based on the Steane code in trapped-ion systems. By taking into account detailed and realistic error models in the highly parallel FT quantum circuit, we have found that the crosstalk of parallel gates is a substantial source of noises, which will destroy the advantage of FT over non-FT circuit implementation. Our detailed study shows, to demonstrate FT quantum logical advantage, it is sufficient to lower the crosstalk error rate p_c below the FT threshold $p^{\mathrm{thres}} = 10^{-6}$ and the infidelity of MS gate δF below $\delta F^{\mathrm{thres}} = 1.86 \times 10^{-3}$, which are conservative for the current parallel QEC cycle of the logical qubit.

To mitigate the crosstalk at the gate level for trapped-ion systems, we have proposed a highly effective scheme to design high-quality parallel gates based on reconfigurable optical tweezer array. We utilize the localized motional modes and the gapped mode frequencies of each pinned

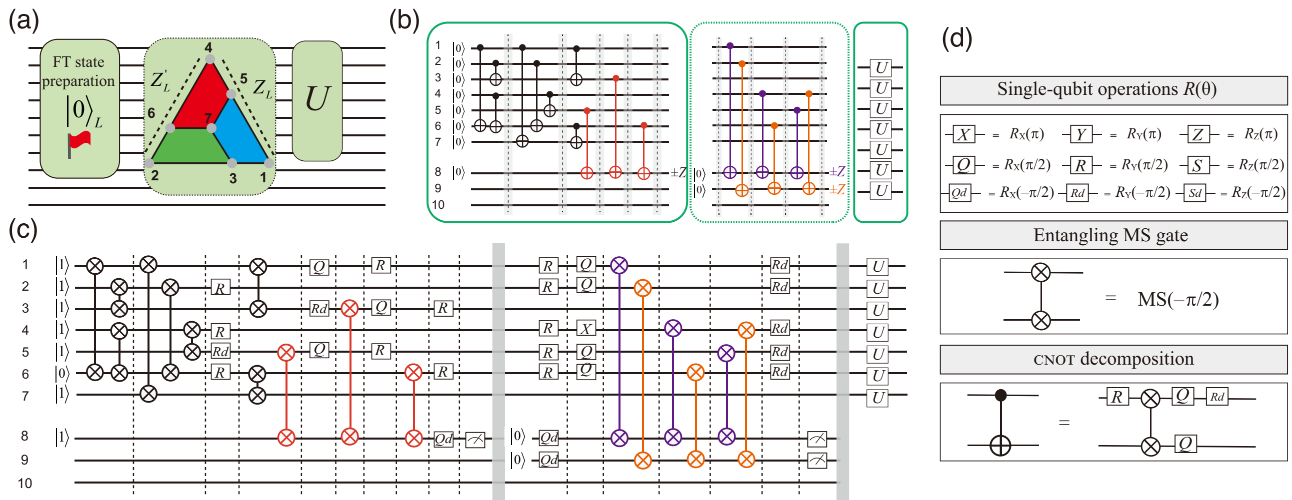

FIG. 10. FT state preparation. (a) We initialize the logical state with a FT protocol using a single ancillary qubit as a flag. If the flag is raised, we measure the logical operates Z'_L, Z''_L to make corrections in Table III. Then, we can rotate $|0\rangle_L$ by applying the logical rotations. (b) The CNOT version of the quantum circuit for (a). (c) The quantum circuit that has been compiled into MS gates with the addition of single-qubit gates. (d) The native gate set consists of single-qubit operations, MS entangling operation, and the decomposition of the CNOT gate into the MS gate and local operations.

ion pair to greatly simplify the crosstalk constraints of optimization. And then we can quickly find the satisfied optical tweezer array for high-quality parallel gates based on a presearch technique. By dynamically reconfiguring the tweezer array, the parallel gate group can be adjusted during running quantum computations, and thus offers great flexibility to achieve FT circuit.

Recently, various platforms have achieved milestone breakthroughs, which exceed the break-even point of the quantum error correction [84,85]. However, the logical error rate needs to be below 10^{-9} on a practical level. Therefore, to achieve the final goal of a practical fault-tolerant quantum computation, it is crucial to scale up the system to improve the code distance and further suppress the noise as we discussed before. However, introducing more qubits to concatenate the QEC code also increases the number of crosstalk errors and the complexity of the QEC circuits when executing more parallel gates.

For different quantum computation platforms, there exist different proper QEC codes. And then the scalability of QEC code size is somewhat different. For the superconducting system with a limited connectivity, the surface code is a natural choice for error correction, because it uses only the nearest-neighbor coupling and rapidly cycled entangling gates. It can increase the qubit number to scale a surface code logical qubit, as shown in Ref. [84]. For the simultaneous gate operations on superconducting qubits, the inevitable crosstalk resulting from the residual interqubit coupling significantly impairs quantum operation performance [40–42]. Reconfigurable neutral atom arrays have recently emerged as a promising quantum computing platform for its high degree of connectivity, as well as a coherent control over hundreds of qubits in a flexible, dynamically reconfigurable architecture [85,86]. It has been demonstrated that an arbitrary connectivity can be established through the coherent atom shuttling by the optical tweezer. This platform features a flexible, dynamically reconfigurable architecture, whereby entangling operations can be performed between neutral-atom qubits with an arbitrary connectivity and in a highly parallel manner. The parallel gate group has negligible crosstalk due to the fact that entangling operations are mediated through Rydberg blockade. In the present work, we have chosen the Steane code due to the all-to-all connectivity of trapped-ion systems. And the operations between qubits are mediated by the motional modes. Based on this advantage, we can adopt concatenation to scale the code size. Therefore, the parallel gates for trapped-ion systems face more serious crosstalk errors when simultaneously executing many two-qubit gates.

In terms of this problem, we may be able to mitigate the crosstalk error when scaling the code size by adopting the following schemes. In the gate level, one interesting study would be combined the parallel gates based on optical tweezers with other techniques to mitigate crosstalk, like the optimization of the ion-qubit mapping to minimize the impact of the crosstalk faults. The authors in Ref. [31] presented a dynamic programming algorithm to find an optimal qubit mapping by searching for Hamiltonian paths in a qubit-mapping graph. In the quantum error-correction code level, it would be helpful to expand the study to other codes, the quantum low-density parity-check (LDPC) code for its the high thresholds and low overhead [87]. As we described, the quantum gate parallelism can speed up the quantum circuit while introducing crosstalk errors. In the quantum circuit level, a trade-off QEC cycle, which balances the need for crosstalk mitigation against the need to parallelism might be helpful [88].

In conclusion, the good combination of the pulse-shape optimization of tweezer parallel quantum gates with fault-tolerant protocol with simultaneous gate operations in circuit design will offer guidance on the application of high-quality parallel quantum gates in error-protected universal quantum computer. Meanwhile, the analysis procedure may provide a preliminary guideline for understanding crosstalk errors of parallel gates in trapped-ion architecture, and may help motivate future work on implementing large-scale FT quantum computers based on the parallel gates.

ACKNOWLEDGMENTS

We thank Ying-Xiang Wang for insightful comments and helpful discussions. This work is supported by National Natural Science Foundation of China Grants No. 12234002 and No. 92250303.

APPENDIX A: OPTIMIZED PULSE SHAPE

In this Appendix, we introduce the approach to obtain the optimized pulse shape for a single MS gate. For a successful completion of an entangling operation, the phase-space trajectories of all motional modes should return to their origins and the qubit states should undergo a maximal entanglement of $\pi/4$ at the end of the gate duration. To fulfill these constraints, we divide the total gate interval τ into N_{seg} segments with an equal time duration of τ/N_{seg}. Thus, we define a real column vector $\mathbf{\Omega} = (\Omega_1, \Omega_2, \ldots, \Omega_{N_{\text{seg}}})^T$, corresponding to the Rabi frequency of each segment and treat the amplitude in each segment as an independent variable. The matrix form of the constraints in Eqs. (4) and (5) can be given as follows:

$$\mathbf{M}^j\mathbf{\Omega}^j = \mathbf{0}, \tag{A1}$$

$$\theta_{j,j'}(\tau) = (\mathbf{\Omega}^j)^T\mathbf{D}^{[j,j']}\mathbf{\Omega}^{j'}, \tag{A2}$$

where $\mathbf{M}^j$ is the $2N \times N_{\text{seg}}$ real coefficient matrix, $\mathbf{D}^{[j,j']}$ is the $N_{\text{seg}} \times N_{\text{seg}}$ matrix, and $\mathbf{\Omega}^j$ is the amplitude vector of length N_{seg} of the jth qubit. The explicit expressions of $\mathbf{M}^j$ and $\mathbf{D}^{[j,j']}$ are given in Refs. [19,61]. In this work, the parameters of two ions in the same MS gate $[j,j']$ are the same, i.e., the detuning $\mu_j = \mu_{j'} = \mu_{[j,j']}$, the gate duration $\tau_j = \tau_{j'} = \tau_{[j,j']}$, the pulse segments $N_{\text{seg}}^j = N_{\text{seg}}^{j'} = N_{\text{seg}}^{[j,j']}$ and the pulse shape $\mathbf{\Omega}^j = \mathbf{\Omega}^{j'} = \mathbf{\Omega}^{[j,j']}$.

As can be seen, the spin-motion decoupling constraints are linear while the coupling strength constraints are quadratic. According to Ref. [52], in the limit of small $\alpha_j^m(\tau)$ and $\alpha_{j'}^m(\tau)$, which means a high fidelity, the infidelity can be approximated as Eq. (11). According to Eq. (A1), the infidelity can be expressed as

$$\begin{aligned}\delta F_{[j,j']} &= \frac{4}{5}\sum_m\left(\left|\alpha_j^m\right|^2 + \left|\alpha_{j'}^m\right|^2\right)(2\bar{n}_m + 1)\\ &= \frac{4}{5}\{(\mathbf{\Omega}^j)^T(\mathbf{M}^j)^\dagger\mathbf{M}^j\mathbf{\Omega}^j + (\mathbf{\Omega}^{j'})^\dagger(\mathbf{M}^{j'})^\dagger\mathbf{M}^{j'}\mathbf{\Omega}^{j'}\}\\ &= \frac{4}{5}\{(\mathbf{\Omega}^{[j,j']})^T(\mathbf{M}^{[j,j']})^\dagger\mathbf{M}^{[j,j']}\mathbf{\Omega}^{[j,j']}\},\end{aligned} \tag{A3}$$

where $\mathbf{\Omega}^j = \mathbf{\Omega}^{j'} = \mathbf{\Omega}^{[j,j']}$ is the discrete pulse sequences of ion pair $[j,j']$ and $\mathbf{M}^{[j,j']} = (\mathbf{M}^j)^\dagger\mathbf{M}^j + (\mathbf{M}^{j'})^\dagger\mathbf{M}^{j'}$.

Therefore, we wish to minimize the spin-motion decoupling under the coupling strength quadratic constraint. Now, one can formulate the constrained optimization problem as

$$\begin{cases} f(\mathbf{\Omega}^{[j,j']}) = \min((\mathbf{\Omega}^{[j,j']})^T(\mathbf{M}^{[j,j']})^\dagger\mathbf{M}^{[j,j']}\mathbf{\Omega}^{[j,j']}),\\ \text{s.t. } \left|(\mathbf{\Omega}^{[j,j']})^T\mathbf{D}^{[j,j']}\mathbf{\Omega}^{[j,j']}\right| = \dfrac{\pi}{4}. \end{cases} \tag{A4}$$

Here, we use the method of Lagrange multiplier to solve this generalized eigenvalue problem and find the eigenvalue with the smallest absolute value. The corresponding eigenvector, with suitable normalization of the spin-spin phase constraint, gives us the optimal pulse shape.

APPENDIX B: FT STATE PREPARATION

The preparation of FT state depicted in the first block of Fig. 4 is achieved by the verification circuit consisting of three additional CNOT gates that couple the data qubits to an ancillary flag qubit [67]. As depicted in Fig. 10, one can detect a correlated error when the flag qubit in the Z basis $M_f = -1$ is measured, which means the flag is triggered. In the postselection method, the state is discarded and the circuit runs again when the flag is triggered. In this work, we adopt an alternative protocol for deterministic FT Pauli-state preparation [38]. This protocol can distinguish the dangerous correlated errors and make a recovery operation, which relies on the combination of the flag measurement and additional measurements of the logical operators $Z_L' = Z_1Z_4Z_5$ and $Z_L'' = Z_2Z_4Z_6$ as detailed in Table III. We can ascertain that after the corrections, fault tolerance at level 1 is achieved without any postselection. For the measurements of the logical operators $Z_L' = Z_1Z_4Z_5$ and $Z_L'' = Z_2Z_4Z_6$, we choose to simultaneously extract them. The quantum circuit of the MS gate version is shown in Fig. 10(c). The gate compilation of the CNOT gate using the MS gate and single-qubit rotations is shown in Fig. 10(d).

TABLE III. When the flag is trigged, one can correct the errors by measuring the two equivalent logical operators Z'_L and Z''_L. The syndromes and corresponding corrections are listed below.

(Z'_L, Z''_L)	$(+1,+1)$	$(+1,-1)$	$(-1,+1)$	$(-1,-1)$
Errors	X_3, X_f	X_6X_7, X_6	X_1X_3, X_5	Higher weight
Correction	I	X_6	X_5	I

APPENDIX C: SERIAL SCHEME

Now, let us compare the results of the QEC protocol based on parallel two-qubit gates with the serial scheme to highlight the parallel advantage in FT computation and estimate the FT threshold of crosstalk. In the serial scheme, the quantum operations are executed sequentially in time and the stabilizers in syndrome measurements are also measured sequentially, which measure only one stabilizer at a time.

The syndrome extraction protocol in the serial scheme can be expressed as follows. If the flag is triggered (i.e., projective measurement in the Z basis $M_f = -1$), one can determine and correct the most likely errors including the dangerous “hook errors” by performing a subsequent unflagged measurement of the three conjugate stabilizers. If, on the other hand, the flag is not triggered, but the syndrome qubit signals an error $M_s = -1$, we can be certain that an error must have occurred on a single qubit at FT level 1. Therefore, we can use the unflagged circuits to extract the syndrome by measuring all stabilizers, and to correct the possible single-qubit error. In both cases, the readout finishes after the unflagged stabilizer measurements. If no flag is triggered, and no error is detected in the syndrome qubit, one can proceed to the next stabilizer with flagged circuit. The details of the serial scheme can be found in Refs. [38,71].

APPENDIX D: THE MS-BASED QUANTUM CIRCUIT OF PARALLEL SYNDROME EXTRACTION

In our work, we make use of the recently introduced paradigm of flag-fault tolerance with the parallel execution of gate operations, where the presence of dangerous errors is heralded by the use of auxiliary flag qubits [39]. In this scheme, each ancillary qubit is used to measure one of the stabilizers, but at the same time acts as a flag to indicate potentially dangerous faults happening on the other ancillary qubits, which otherwise could propagate onto several data qubits and cause a logical error. The MS-based quantum circuit of parallel syndrome extraction with three stabilizers is shown in Fig. 11.

APPENDIX E: DECODER FOR X-TYPE ERRORS

The lookup decoders for X-type errors are shown in Tables IV and V. For example, for the X errors that can trigger one or both Z measurements in Fig. 5(a), X_4 and X_3X_7 are not distinguishable from the unflagged stabilizer measurements with $\{S_Z^{(1)}, S_Z^{(2)}, S_Z^{(3)}\} = [-,+,+]$. However, X_4 can occur only with $\{S_X^{(3)f}, S_Z^{(1)f}, S_Z^{(2)f}\} = [+,-,+]$ measurements, while X_3X_7 can occur only with $[+,-,-]$ measurements, so a special correction rule is only needed in the latter case.

TABLE IV. Decoder for X-type weight-two single-qubit errors.

$S_X^{(3)f}, S_Z^{(1)f}, S_Z^{(2)f}$	$S_Z^{(1)}, S_Z^{(2)}, S_Z^{(3)}$	Correction
$+--$	$-++$	X_3X_7
$---$	$-++$	X_3X_7
$S_Z^{(3)f}, S_X^{(1)f}, S_X^{(2)f}$	$S_Z^{(1)}, S_Z^{(2)}, S_Z^{(3)}$	Correction
$-++$	$+-+$	X_4X_6
$--+$	$+-+$	X_4X_6
$-++$	$-++$	X_3X_7
$-+-$	$-++$	X_3X_7

APPENDIX F: LOCALIZED MOTIONAL MODES OF THE TWEEZER ARRAY

For a Gaussian optical tweezer propagating along the y direction, the optical dipole potential can be approximated as harmonic in the vicinity of the focuses of the tweezers by considering the tweezer intensity profile at each ion, being centered at each corresponding equilibrium position. As shown in Ref. [47], the optical trapping frequency along the beam axis y compared to the other axis is negligible. In contrast, the optical trapping frequency along the transverse x and the longitudinal z directions is determined by the tweezer intensity ω_i^{tw} centered at the position of the ith ion. The addition of Φ_{tweezer} does not modify the equilibrium position of the ions since its gradient vanishes there.

In order to characterize the effect of the tweezer potential on the motional modes and mode frequencies, we consider N ions, which are confined by the harmonic trapping

TABLE V. Decoder for weight-one “nonhook errors.”

$S_Z^{(1)}, S_Z^{(2)}, S_Z^{(3)}$	Correction
$+++$	I
$++-$	X_1
$+-+$	X_2
$+--$	X_3
$-++$	X_4
$-+-$	X_5
$--+$	X_6
$---$	X_7

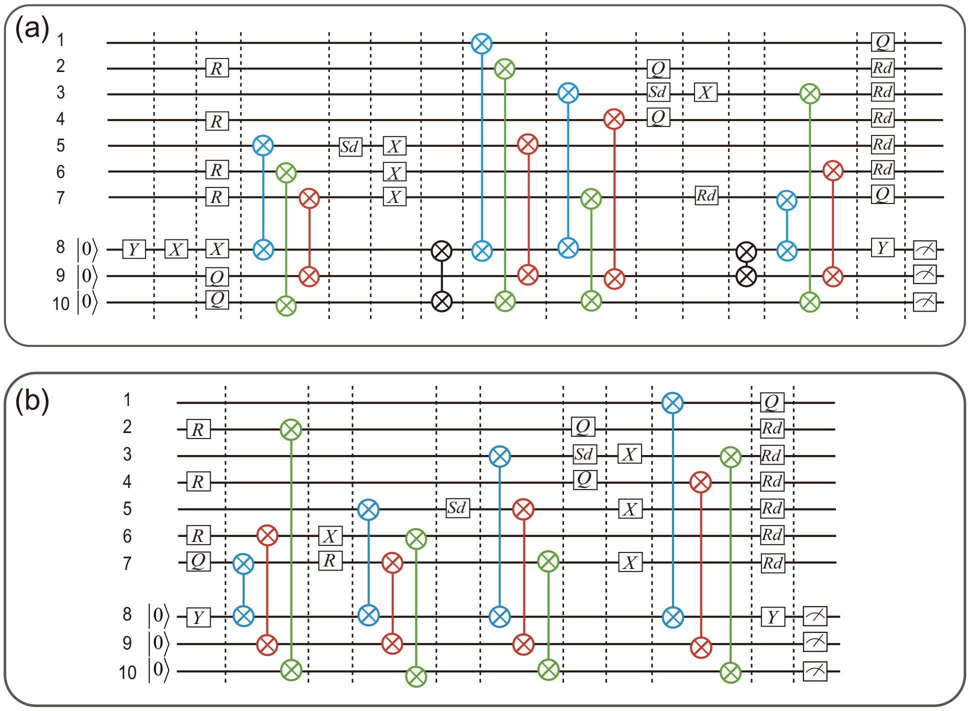

FIG. 11. (a) The MS-based first parallel flagged syndrome extraction of the stabilizers $\{S_X^{(3)f}, S_Z^{(1)f}, S_Z^{(2)f}\}$ with entangling MS gates and single-qubit rotations for Fig. 5(a). (b) The MS-based first parallel unflagged syndrome extraction of the stabilizers $\{S_X^{(3)}, S_Z^{(1)}, S_Z^{(2)}\}$ for Fig. 5(b).

potential and the total potential has the following form:

$$U_{\text{all}} = \sum_{i=1}^{N}\left(\frac{1}{2}m_{\text{ion}}^{i}\omega_x^2 x_i^2 + \frac{1}{2}m_{\text{ion}}^{i}\omega_y^2 y_i^2 + \frac{1}{2}m_{\text{ion}}^{i}\omega_z^2 z_i^2\right) + \sum_{i=1}^{N}\left(\frac{1}{2}m_{\text{ion}}^{i}\omega_i^{\text{tw}2}x_i^2 + \frac{1}{2}m_{\text{ion}}^{i}\omega_i^{\text{tw}2}z_i^2\right) + \sum_{i<j}\frac{q^2}{4\pi\varepsilon_0|\mathbf{r}_i - \mathbf{r}_j|}, \tag{F1}$$

where q is the charge of an ion, z_i is the axial position of the ith ion, N is the number of ions, ε_0 is the permittivity of free space, $x_i^{(0)} = y_i^{(0)} = 0, z_i^{(0)} = l_0 u_i^{(0)}$, m_{ion}^i is the mass of ion, and ω_x and ω_y are the radial trap frequencies. ω_i^{tw} denotes the local optical pinning curvature at the ith ion. For convenience, we rescale the positions z_i using a length scale $l_0{}^3 = q^2/4\pi\varepsilon_0 m_{\text{ion}}\omega_z^2$ and then $u_i = z_i/l_0$.

We can approximate the potential with its Taylor expansion around the equilibrium positions up to the second order. The dynamics of the system are described by the Lagrangian

$$L = \frac{1}{2}m_{\text{ion}}\sum_{i=1}^{N}(\dot{q}_i)^2 - \frac{1}{2}m_{\text{ion}}\sum_{i,j=1}^{N}A_{ij}q_i q_j, \tag{F2}$$

where q_i is the displacement of the ith ion from the equilibrium position. The motional modes and their corresponding mode frequencies can be obtained through diagonalization of the symmetric Hessian matrix A_{ij} of the potential energy.

Using Eq. (F1), one can obtain the analytical expression $A_{ij}^{(x)}$ for the transverse motion

$$\frac{\partial^2 U}{\partial x_i^2}\Big|_{\mathbf{r}=\mathbf{r}^{(0)}} = \omega_x^2 + (\omega_i^{\text{tw}})^2 - \sum_{i\neq j}\frac{\omega_z^2}{|u_{ij}|^3}, \tag{F3}$$

$$\frac{\partial^2 U}{\partial x_i \partial x_j}\Big|_{\mathbf{r}=\mathbf{r}^{(0)}} = \frac{\omega_z^2}{|u_{ij}|^3}, \quad i \neq j, \tag{F4}$$

where $u_{ij} = u_i - u_j$. The eigenvectors b_j^m are defined by $\sum_{i=1}^{N} A_{ij} b_i^m = \omega_m^2 b_j^m$, where ω_m is the transverse motional mode frequency with $m = 1, \ldots, N$ being the motional mode index. Each motional mode represents an individual harmonic oscillator that can be quantized to give the phonon Hamiltonian. As stated above, among the contributions to the diagonal elements of mode matrices, the conventional harmonic trapping potential allows for an identical trapping potential for all ions of the same mass and charge. On the other hand, optical tweezers on individual ions give control over site-dependent trapping strengths.

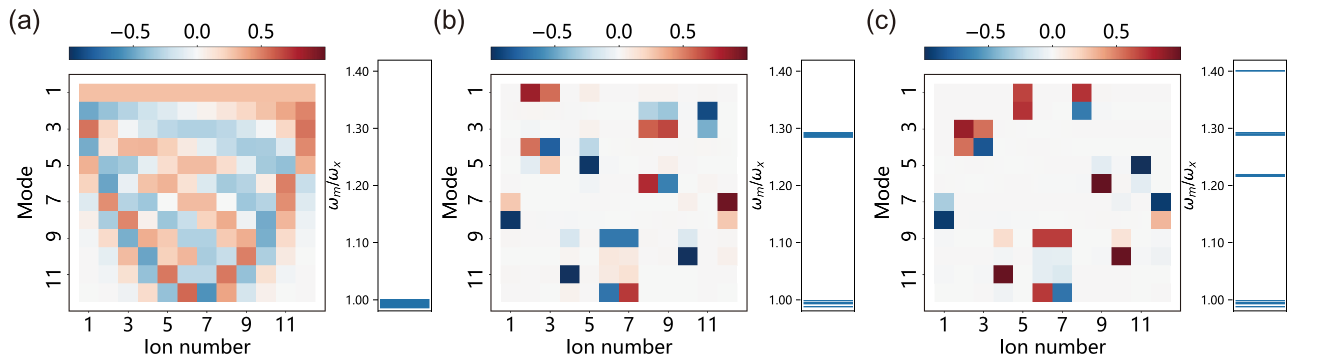

FIG. 12. (a) The x transverse motional modes b_j^m, $j,m=1,\ldots,12$ of ion chain without tweezers. The oscillation amplitude and direction of ions are represented by the color of the squares. The mode-frequency spectrum ω_m/ω_x is shown on the right side. (b) The transverse motional modes and mode frequencies of ion chain in an array of programmable optical tweezers $\{\omega^{\mathrm{tw}}_{[2,3]},\omega^{\mathrm{tw}}_{[5,8]},\omega^{\mathrm{tw}}_{[9,11]}\}=\{0.821\omega_x,0.821\omega_x,0.821\omega_x\}$ for parallel gate group $\{[2,3],[5,8],[9,11]\}$. (c) The transverse motional modes and mode frequencies of ion chain in an array of programmable optical tweezers $\{\omega^{\mathrm{tw}}_{[2,3]},\omega^{\mathrm{tw}}_{[5,8]},\omega^{\mathrm{tw}}_{[9,11]}\}=\{0.821\omega_x,0.989\omega_x,0.703\omega_x\}$ for parallel gate group $\{[2,3],[5,8],[9,11]\}$.

As an example, we consider a chain of $N=12$ ions and present the motional modes and mode frequencies in the presence of optical tweezer array with different intensity and, for comparison, with same intensity and without tweezers as depicted Fig. 12. As we can see in Fig. 12(a), all ions oscillate in the motional modes due to all-to-all interaction, which induce the crosstalk of parallel gates. However, the collective modes of the ion chain are modified by the additional tweezer potentials as depicted in Figs. 12(b) and 12(c). In the regime of strong pinning, the motion of pinned ions decouple from other ions along the x direction so that the motional modes of the pinned ions are localized and independent. The dense mode frequencies of the ion chain are gapped and split up into several subsets. However, in the scheme that all ions are pinned with the same optical trapping frequency, their localized modes hybridize and the mode frequencies of parallel ion pairs are crowded together, which is in principle not desirable in Fig. 12(b). Therefore, we choose the tweezer array with different strengths in which the crosstalk of each ion pair is naturally suppressed. We can engineer specific types of motional modes and the corresponding frequencies by using optical tweezer array that are focused on specific ions and thus pin these ions.

[1] P. W. Shor, Polynomial-time algorithms for prime factorization and discrete logarithms on a quantum computer, SIAM Rev. **41**, 303 (1999).
[2] R. P. Feynman, Simulating physics with computers, Int. J. Theor. Phys. **21**, 467 (1982).
[3] A. R. Calderbank and P. W. Shor, Good quantum error-correcting codes exist, Phys. Rev. A **54**, 1098 (1996).
[4] A. M. Steane, Error correcting codes in quantum theory, Phys. Rev. Lett. **77**, 793 (1996).
[5] P. W. Shor, Scheme for reducing decoherence in quantum computer memory, Phys. Rev. A **52**, R2493 (1995).
[6] B. M. Terhal, Quantum error correction for quantum memories, Rev. Mod. Phys. **87**, 307 (2015).
[7] J. I. Cirac and P. Zoller, Quantum computations with cold trapped ions, Phys. Rev. Lett. **74**, 4091 (1995).
[8] C. D. Bruzewicz, J. Chiaverini, R. McConnell, and J. M. Sage, Trapped-ion quantum computing: Progress and challenges, Appl. Phys. Rev. **6**, 021314 (2019).
[9] W. Chen, J. Gan, J.-N. Zhang, D. Matuskevich, and K. Kim, Quantum computation and simulation with vibrational modes of trapped ions, Chin. Phys. B **30**, 060311 (2021).
[10] P. Wang, C.-Y. Luan, M. Qiao, M. Um, J. Zhang, Y. Wang, X. Yuan, M. Gu, J. Zhang, and K. Kim, Single ion qubit with estimated coherence time exceeding one hour, Nat. Commun. **12**, 233 (2021).
[11] T. P. Harty, D. T. C. Allcock, C. J. Ballance, L. Guidoni, H. A. Janacek, N. M. Linke, D. N. Stacey, and D. M. Lucas, High-fidelity preparation, gates, memory, and readout of a trapped-ion quantum bit, Phys. Rev. Lett. **113**, 220501 (2014).
[12] C. J. Ballance, T. P. Harty, N. M. Linke, M. A. Sepiol, and D. M. Lucas, High-fidelity quantum logic gates using trapped-ion hyperfine qubits, Phys. Rev. Lett. **117**, 060504 (2016).
[13] J. P. Gaebler, T. R. Tan, Y. Lin, Y. Wan, R. Bowler, A. C. Keith, S. Glancy, K. Coakley, E. Knill, D. Leibfried, *et al.* High-fidelity universal gate set for $^{9}Be^{+}$ ion qubits, Phys. Rev. Lett. **117**, 060505 (2016).
[14] C. R. Clark, H. N. Tinkey, B. C. Sawyer, A. M. Meier, K. A. Burkhardt, C. M. Seck, C. M. Shappert, N. D. Guise, C. E. Volin, S. D. Fallek, *et al.*, High-fidelity Bell-state preparation with $^{40}Ca^{+}$ optical qubits, Phys. Rev. Lett. **127**, 130505 (2021).
[15] C. Figgatt, A. Ostrander, N. M. Linke, K. A. Landsman, D. Zhu, D. Maslov, and C. Monroe, Parallel entangling operations on a universal ion-trap quantum computer, Nature **572**, 368 (2019).

[16] Y. Lu, S. Zhang, K. Zhang, W. Chen, Y. Shen, J. Zhang, J.-N. Zhang, and K. Kim, Global entangling gates on arbitrary ion qubits, Nature **572**, 363 (2019).

[17] C. D. B. Bentley, H. Ball, M. J. Biercuk, A. R. R. Carvalho, M. R. Hush, and H. J. Slatyer, Numeric optimization for configurable, parallel, error-robust entangling gates in large ion registers, Adv. Quantum Technol. **3**, 2000044 (2020).

[18] N. Grzesiak, R. Blümel, K. Wright, K. M. Beck, N. C. Pisenti, M. Li, V. Chaplin, J. M. Amini, S. Debnath, J.-S. Chen, *et al.*, Efficient arbitrary simultaneously entangling gates on a trapped-ion quantum computer, Nat. Commun. **11**, 2963 (2020).

[19] L. Cheng, S.-C. Liu, G.-Z. Yao, Y.-X. Wang, L.-Y. Peng, and Q. Gong, High-quality parallel entangling gates in long mixed-species ion chains, Phys. Rev. A **108**, 042603 (2023).

[20] D. Nigg, M. Müller, E. A. Martinez, P. Schindler, M. Hennrich, T. Monz, M. A. Martin-Delgado, and R. Blatt, Quantum computations on a topologically encoded qubit, Science **345**, 302 (2014).

[21] J. Hilder, D. Pijn, O. Onishchenko, A. Stahl, M. Orth, B. Lekitsch, A. Rodriguez-Blanco, M. Müller, F. Schmidt-Kaler, and U. G. Poschinger, Fault-tolerant parity readout on a shuttling-based trapped-ion quantum computer, Phys. Rev. X **12**, 011032 (2022).

[22] L. Egan, D. M. Debroy, C. Noel, A. Risinger, D. Zhu, D. Biswas, M. Newman, M. Li, K. R. Brown, M. Cetina, *et al.*, Fault-tolerant control of an error-corrected qubit, Nature **598**, 281 (2021).

[23] L. Postler, S. Heußen, I. Pogorelov, M. Rispler, T. Feldker, M. Meth, C. D. Marciniak, R. Stricker, M. Ringbauer, R. Blatt, *et al.*, Demonstration of fault-tolerant universal quantum gate operations, Nature **605**, 675 (2022).

[24] A. Erhard, H. Poulsen Nautrup, M. Meth, L. Postler, R. Stricker, M. Stadler, V. Negnevitsky, M. Ringbauer, P. Schindler, H. J. Briegel, *et al.*, Entangling logical qubits with lattice surgery, Nature **589**, 220 (2021).

[25] C. Ryan-Anderson, J. G. Bohnet, K. Lee, D. Gresh, A. Hankin, J. Gaebler, D. Francois, A. Chernoguzov, D. Lucchetti, N. C. Brown, *et al.*, Realization of real-time fault-tolerant quantum error correction, Phys. Rev. X **11**, 041058 (2021).

[26] C. Ryan-Anderson, N. C. Brown, M. S. Allman, B. Arkin, G. Asa-Attuah, C. Baldwin, J. Berg, J. G. Bohnet, S. Braxton, N. Burdick, *et al.*, Implementing fault-tolerant entangling gates on the five-qubit code and the color code, arXiv:2208.01863.

[27] L. Postler, F. Butt, I. Pogorelov, C. D. Marciniak, S. Heußen, R. Blatt, P. Schindler, M. Rispler, M. Müller, and T. Monz, Demonstration of fault-tolerant Steane quantum error correction, PRX Quantum **5**, 030326 (2024).

[28] A. Bermudez, X. Xu, R. Nigmatullin, J. O'Gorman, V. Negnevitsky, P. Schindler, T. Monz, U. G. Poschinger, C. Hempel, J. Home, *et al.*, Assessing the progress of trapped-ion processors towards fault-tolerant quantum computation, Phys. Rev. X **7**, 041061 (2017).

[29] S. Heußen, L. Postler, M. Rispler, I. Pogorelov, C. D. Marciniak, T. Monz, P. Schindler, and M. Müller, Strategies for a practical advantage of fault-tolerant circuit design in noisy trapped-ion quantum computers, Phys. Rev. A **107**, 042422 (2023).

[30] P. Parrado-Rodríguez, C. Ryan-Anderson, A. Bermudez, and M. Müller, Crosstalk suppression for fault-tolerant quantum error correction with trapped ions, Quantum **5**, 487 (2021).

[31] D. M. Debroy, M. Li, S. Huang, and K. R. Brown, Logical performance of 9 qubit compass codes in ion traps with crosstalk errors, Quantum Sci. Technol. **5**, 034002 (2020).

[32] C. Fang, Y. Wang, S. Huang, K. R. Brown, and J. Kim, Crosstalk suppression in individually addressed two-qubit gates in a trapped-ion quantum computer, Phys. Rev. Lett. **129**, 240504 (2022).

[33] R.-R. Li, Y.-L. Chen, R. He, S.-Q. Chen, W.-H. Qi, J.-M. Cui, Y.-F. Huang, C.-F. Li, and G.-C. Guo, A low-crosstalk double-side addressing system using acousto-optic deflectors for atomic ion qubits, arXiv:2306.01307.

[34] Y.-H. Hou, Y.-J. Yi, Y.-K. Wu, Y.-Y. Chen, L. Zhang, Y. Wang, Y.-L. Xu, C. Zhang, Q.-X. Mei, H.-X. Yang, *et al.*, Individually addressed entangling gates in a two-dimensional ion crystal, arXiv:2406.13999.

[35] R. Chao and B. W. Reichardt, Quantum error correction with only two extra qubits, Phys. Rev. Lett. **121**, 050502 (2018).

[36] M. Li, M. Gutiérrez, S. E. David, A. Hernandez, and K. R. Brown, Fault tolerance with bare ancillary qubits for a [[7,1,3]] code, Phys. Rev. A **96**, 032341 (2017).

[37] C. Chamberland and M. E. Beverland, Flag fault-tolerant error correction with arbitrary distance codes, Quantum **2**, 53 (2018).

[38] A. Bermudez, X. Xu, M. Gutiérrez, S. C. Benjamin, and M. Müller, Fault-tolerant protection of near-term trapped-ion topological qubits under realistic noise sources, Phys. Rev. A **100**, 062307 (2019).

[39] B. W. Reichardt, Fault-tolerant quantum error correction for Steane's seven-qubit color code with few or no extra qubits, Quantum Sci. Technol. **6**, 015007 (2020).

[40] A. Ketterer and T. Wellens, Characterizing crosstalk of superconducting transmon processors, Phys. Rev. Appl. **20**, 034065 (2023).

[41] P. Zhao, K. Linghu, Z. Li, P. Xu, R. Wang, G. Xue, Y. Jin, and H. Yu, Quantum crosstalk analysis for simultaneous gate operations on superconducting qubits, PRX Quantum **3**, 020301 (2022).

[42] Y. Liang, M.-J. Liang, S. Li, Z. D. Wang, and Z.-Y. Xue, Scalable protocol to mitigate *zz* crosstalk in universal quantum gates, Phys. Rev. Appl. **21**, 024016 (2024).

[43] T. Olsacher, L. Postler, P. Schindler, T. Monz, P. Zoller, and L. M. Sieberer, Scalable and parallel tweezer gates for quantum computing with long ion strings, PRX Quantum **1**, 020316 (2020).

[44] D. Schwerdt, L. Peleg, Y. Shapira, N. Priel, Y. Florshaim, A. Gross, A. Zalic, G. Afek, N. Akerman, A. Stern, *et al.*, Scalable architecture for trapped-ion quantum computing using RF traps and dynamic optical potentials, arXiv:2311.01168.

[45] M. Mazzanti, R. Gerritsma, R. J. C. Spreeuw, and A. Safavi-Naini, Trapped ions quantum logic gate with optical tweezers and the Magnus effect, Phys. Rev. Res. **5**, 033036 (2023).

[46] Y.-C. Shen and G.-D. Lin, Scalable quantum computing stabilised by optical tweezers on an ion crystal, New J. Phys. **22**, 053032 (2020).

[47] Y. H. Teoh, M. Sajjan, Z. Sun, F. Rajabi, and R. Islam, Manipulating phonons of a trapped-ion system using optical tweezers, Phys. Rev. A **104**, 022420 (2021).

[48] W. C. Campbell, J. Mizrahi, Q. Quraishi, C. Senko, D. Hayes, D. Hucul, D. N. Matsukevich, P. Maunz, and C. Monroe, Ultrafast gates for single atomic qubits, Phys. Rev. Lett. **105**, 090502 (2010).

[49] A. Sørensen and K. Mølmer, Entanglement and quantum computation with ions in thermal motion, Phys. Rev. A **62**, 022311 (2000).

[50] S.-L. Zhu, C. Monroe, and L.-M. Duan, Arbitrary-speed quantum gates within large ion crystals through minimum control of laser beams, Europhys. Lett. **73**, 485 (2006).

[51] S.-L. Zhu, C. Monroe, and L.-M. Duan, Trapped ion quantum computation with transverse phonon modes, Phys. Rev. Lett. **97**, 050505 (2006).

[52] Y. Wu, S.-T. Wang, and L.-M. Duan, Noise analysis for high-fidelity quantum entangling gates in an anharmonic linear Paul trap, Phys. Rev. A **97**, 062325 (2018).

[53] T. J. Green and M. J. Biercuk, Phase-modulated decoupling and error suppression in qubit-oscillator systems, Phys. Rev. Lett. **114**, 120502 (2015).

[54] A. R. Milne, C. L. Edmunds, C. Hempel, F. Roy, S. Mavadia, and M. J. Biercuk, Phase-modulated entangling gates robust to static and time-varying errors, Phys. Rev. Appl. **13**, 024022 (2020).

[55] S.-C. Liu, L. Cheng, G.-Z. Yao, Y.-X. Wang, and L.-Y. Peng, Efficient numerical approach to high-fidelity phase-modulated gates in long chains of trapped ions, Phys. Rev. E **107**, 035304 (2023).

[56] P. H. Leung, K. A. Landsman, C. Figgatt, N. M. Linke, C. Monroe, and K. R. Brown, Robust 2-qubit gates in a linear ion crystal using a frequency-modulated driving force, Phys. Rev. Lett. **120**, 020501 (2018).

[57] M. Kang, Y. Wang, C. Fang, B. Zhang, O. Khosravani, J. Kim, and K. R. Brown, Designing filter functions of frequency-modulated pulses for high-fidelity two-qubit gates in ion chains, Phys. Rev. Appl. **19**, 014014 (2023).

[58] M. Kang, Q. Liang, B. Zhang, S. Huang, Y. Wang, C. Fang, J. Kim, and K. R. Brown, Batch optimization of frequency-modulated pulses for robust two-qubit gates in ion chains, Phys. Rev. Appl. **16**, 024039 (2021).

[59] P. H. Leung and K. R. Brown, Entangling an arbitrary pair of qubits in a long ion crystal, Phys. Rev. A **98**, 032318 (2018).

[60] R. Blümel, N. Grzesiak, N. Pisenti, K. Wright, and Y. Nam, Power-optimal, stabilized entangling gate between trapped-ion qubits, npj Quantum Inf. **7**, 147 (2021).

[61] L. Cheng, S.-C. Liu, L. Geng, Y.-K. Fang, and L.-Y. Peng, Robust segmented entangling gates with pulse gradient and power optimization using a hypersurface-tangent method, Phys. Rev. A **107**, 042617 (2023).

[62] C. J. Trout, M. Li, M. Gutiérrez, Y. Wu, S.-T. Wang, L. Duan, and K. R. Brown, Simulating the performance of a distance-3 surface code in a linear ion trap, New J. Phys. **20**, 043038 (2018).

[63] H. Bombin and M. A. Martin-Delgado, Topological quantum distillation, Phys. Rev. Lett. **97**, 180501 (2006).

[64] M. A. Nielsen and I. L. Chuang, *Quantum Computation and Quantum Information* (Cambridge University Press, Cambridge, UK, 2010).

[65] S. Bravyi and A. Kitaev, Universal quantum computation with ideal Clifford gates and noisy ancillas, Phys. Rev. A **71**, 022316 (2005).

[66] C. Chamberland and A. W. Cross, Fault-tolerant magic state preparation with flag qubits, Quantum **3**, 143 (2019).

[67] H. Goto, Minimizing resource overheads for fault-tolerant preparation of encoded states of the Steane code, Sci. Rep. **6**, 19578 (2016).

[68] D. P. DiVincenzo and P. W. Shor, Fault-tolerant error correction with efficient quantum codes, Phys. Rev. Lett. **77**, 3260 (1996).

[69] A. M. Steane, Active stabilization, quantum computation, and quantum state synthesis, Phys. Rev. Lett. **78**, 2252 (1997).

[70] E. Knill, Quantum computing with realistically noisy devices, Nature **434**, 39 (2005).

[71] M. Gutiérrez, M. Müller, and A. Bermúdez, Transversality and lattice surgery: Exploring realistic routes toward coupled logical qubits with trapped-ion quantum processors, Phys. Rev. A **99**, 022330 (2019).

[72] C. Ryan-Anderson, PECOS: Performance estimator of codes on surfaces (2019).

[73] C. Ryan-Anderson, *Quantum algorithms, architecture, and error correction*, Ph.D. thesis, The University of New Mexico (2018).

[74] D. Gottesman, Quantum fault tolerance in small experiments, arXiv:1610.03507.

[75] Z.-Z. Liu and Y. Wang, Handling constrained multiobjective optimization problems with constraints in both the decision and objective spaces, IEEE Trans. Evol. Comput. **23**, 870 (2019).

[76] C. Zhu, R. H. Byrd, P. Lu, and J. Nocedal, Algorithm 778: L-BFGS-B: Fortran subroutines for large-scale bound-constrained optimization, ACM Trans. Math. Softw. **23**, 550 (1997).

[77] S.-A. Guo, Y.-K. Wu, J. Ye, L. Zhang, W.-Q. Lian, R. Yao, Y. Wang, R.-Y. Yan, Y.-J. Yi, Y.-L. Xu, *et al.*, A site-resolved two-dimensional quantum simulator with hundreds of trapped ions, Nature **630**, 613 (2024).

[78] M. Qiao, Z. Cai, Y. Wang, B. Du, N. Jin, W. Chen, P. Wang, C. Luan, E. Gao, X. Sun, *et al.*, Tunable quantum simulation of spin models with a two-dimensional ion crystal, Nat. Phys. **20**, 623 (2024).

[79] D. Kiesenhofer, H. Hainzer, A. Zhdanov, P. C. Holz, M. Bock, T. Ollikainen, and C. F. Roos, Controlling two-dimensional coulomb crystals of more than 100 ions in a monolithic radio-frequency trap, PRX Quantum **4**, 020317 (2023).

[80] S.-T. Wang, C. Shen, and L.-M. Duan, Quantum computation under micromotion in a planar ion crystal, Sci. Rep. **5**, 8555 (2015).

[81] Y.-K. Wu, Z.-D. Liu, W.-D. Zhao, and L.-M. Duan, High-fidelity entangling gates in a three-dimensional ion crystal under micromotion, Phys. Rev. A **103**, 022419 (2021).

[82] P. Richerme, Two-dimensional ion crystals in radio-frequency traps for quantum simulation, Phys. Rev. A **94**, 032320 (2016).

[83] L. Bond, L. Lenstra, R. Gerritsma, and A. Safavi-Naini, Effect of micromotion and local stress in quantum simulations with trapped ions in optical tweezers, Phys. Rev. A **106**, 042612 (2022).

[84] Z. Ni, S. Li, X. Deng, Y. Cai, L. Zhang, W. Wang, Z.-B. Yang, H. Yu, F. Yan, S. Liu, *et al.*, Beating the break-even point with a discrete-variable-encoded logical qubit, Nature **616**, 56 (2023).

[85] D. Bluvstein, S. J. Evered, A. A. Geim, S. H. Li, H. Zhou, T. Manovitz, S. Ebadi, M. Cain, M. Kalinowski, D. Hangleiter, *et al.*, Logical quantum processor based on reconfigurable atom arrays, Nature **626**, 58 (2024).

[86] S. J. Evered, D. Bluvstein, M. Kalinowski, S. Ebadi, T. Manovitz, H. Zhou, S. H. Li, A. A. Geim, T. T. Wang, N. Maskara, *et al.*, High-fidelity parallel entangling gates on a neutral-atom quantum computer, Nature **622**, 268 (2023).

[87] N. P. Breuckmann and J. N. Eberhardt, Quantum low-density parity-check codes, PRX Quantum **2**, 040101 (2021).

[88] P. Murali, D. C. Mckay, M. Martonosi, and A. Javadi-Abhari, in *Proceedings of the Twenty-Fifth International Conference on Architectural Support for Programming Languages and Operating Systems*, ASPLOS '20 (Association for Computing Machinery, New York, NY, USA, 2020), p. 1001.